11•12•2018

ЕЛЕКТРОТЕХНИКА И ЕЛЕКТРОНИКА

ELECTROTECHNICA & ELECTRONICA

E+E

PUBLISHED BY

BULGARIAN UNION OF ELECTRONICS,

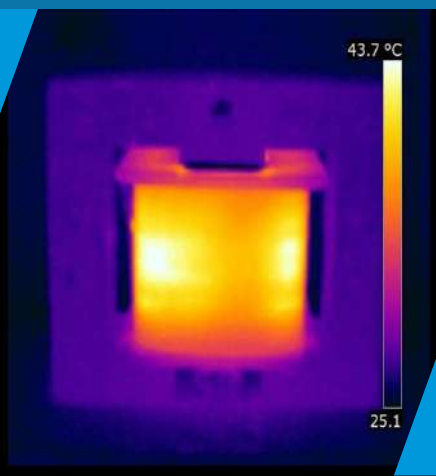

ELECTRICAL ENGINEERING AND

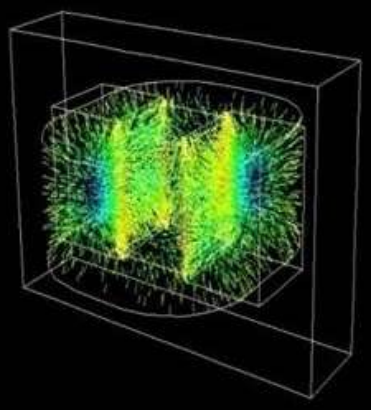

TELECOMMUNICATIONS

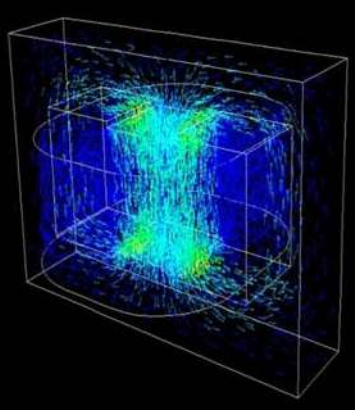

BULGARIA, SOFIA, CEEC.FNTS.BG

ELECTROTECHNICA & ELECTRONICA E+E

Vol. 53. No 11-12/2018

Monthly scientific and technical journal

Published by:

The Union of Electronics, Electrical Engineering and Telecommunications /CEEC/, BULGARIA

Corresponding address:
108 Rakovski St.
Sofia 1000
BULGARIA
Tel. +359 2 987 97 67
e-mail: epluse@mail.bg
http://epluse.fnts.bg

ISSN 0861-4717

C O N T E N T S

In 2018, the journal Electrotechnica & Electronica is published with the financial support of the Scientific Research Fund at the Ministry of Education and Science.

Analysis of typical faults in the real grid of 22 kV Roha town feeder (India)

Vikas Gaikwad, Angel Tcolov, Ivan Yatchev

Abstract-- The fault analysis and evaluation of fault voltage and current in the power system network is very important for a stable and reliable operation of the power system. In the present paper, a study of various reasons for faults in a real grid is carried out and various methods of localizing the fault are also discussed. All the analyses of the faults have being performed on the real grid of 22KV of Roha town feeder. The data of last three years including parameters like time of faults, maximum downtime, voltage before and after the fault, current before and after the fault, power before and after the fault are considered for the analysis. The study undertaken herewith is an attempt to develop a methodology and framework for achieving better and reliable energy supply.

Introduction

The use of electricity increases day by day, whereas technology is developed to utilize electrical energy in an optimal way. Electrical energy is transmitted and distributed from one place to another place via massively interconnected power systems. In power station, electrical energy is generated and for the same power to be transmitted through transmission lines lot of infrastructure, i.e. substations, power stations and power lines are required. These lines are mainly divided into EHV and medium voltage lines. As per the design of equipment, normal current is flowing. Any increase in the current levels of the power systems, this faulty current will flow through the complete equipment. The fault phenomenon affects the complete system dependability, reliability and quality of energy supply.

In 1956, L.W. Coombe and D. G. Lewis proposed the primary fault analysis program. Several exiting texts provide an extensive analysis in fault studies and calculation [1]-[7]. In power system studies, the evaluation of fault analysis is very important. In this paper, we provide three years data of different types of faults, voltages and currents and design of an appropriate protecting scheme for the power system. The main task is to calculate fault conditions and provide protecting equipment designed to isolate the faulty part of lines. Fault analysis is divided into two groups-unsymmetrical and symmetrical faults. In this paper, we discuss only unsymmetrical faults (line to ground, line to line and double line to ground faults). While considering 22kv real grid, some of the common causes of failure of the grid are lightning, high speed wind, earthquakes etc. There may be some accidental faults such as fall of tree branches on lines, vehicles colliding with poles [2].

The process of calculation of system voltages and currents under various types of short-circuiting conditions is called fault analysis. Analysis of fault is required to improve quality and reliability of customer service. Fault current may change from time to time. Therefore a suitable fault analysis method is required for different fault currents, so that new setting of the protective elements takes place. (sectionalize switches, auto reclosers, and fuses). Fault analysis can also be useful to estimate the size of the other fault current limiters or reactors which may be required to be inserted into the system to minimize the short-circuit currents to an optimum safe value which is below the rated capacity of the installed circuit-breakers. Usually, the effect of load is neglected during the short-circuit analysis.

Roha town feeder data

The Roha town feeder data is taken into consideration for our analysis. 100/22 kV sub-station is having 100 kV incomer line and connected to two power transformers of capacity 25 MVA. From the common bus bars of the two transformers 11 feeders are emanating. Out of 11 feeders,4 feeders are shown in Fig. 1. This substation supplies power to Roha town and Dhatav industrial area.

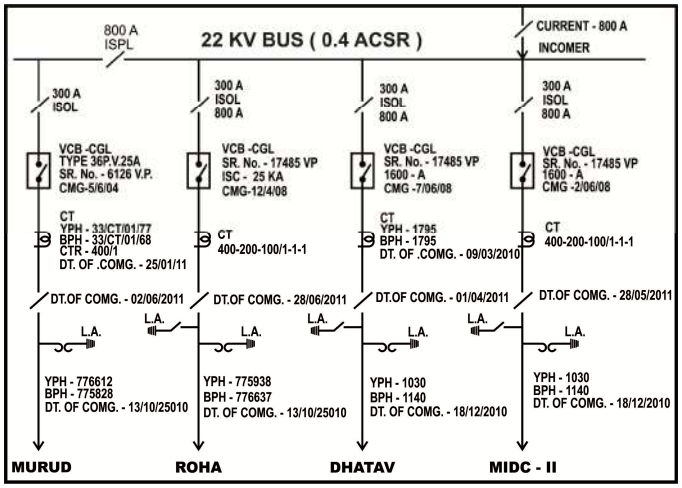

Fig.1. Roha 100kV/22 kV substation.

The subject of consideration in this paper will be one of the feeders, shown in Fig. 2. Relay and the terminal block picture of Roha town feeder are shown in Fig. 3.

Abbreviations used in Fig. 1 and Fig. 2 are listed below:

DTC- Distribution Transforner Center
AB switch- Air Brake Switch
HT- High Tention line
ISOL or ISC- Isolaters
VCB-Vaccume Circuit Breaker
CT-Current Transformer
LA-Lightning Arrester
YPH- Y Phase
BPH- B Phase
CTR-Current Ratio
CGL- Crompton Greaves Ltd.
ACSR- Aluminum Conducted Steel Reinforced

The past three years (2014, 2015 and 2016) data are taken and maintained in an MS Excel sheet with the following parameters.

The subject of consideration in this paper will be one of the feeders, shown in Fig. 2. Relay and the terminal block picture of Roha town feeder are shown in Fig. 3.The past three years (2014, 2015 and 2016) data are taken and maintained in an MS Excel sheet with the following parameters.

1. Tripping time.
2. Duration of Break down.
3. The reason for Break down.
4. Voltage, Current, Power and Frequency before and after tripping.
5. Protection operated.

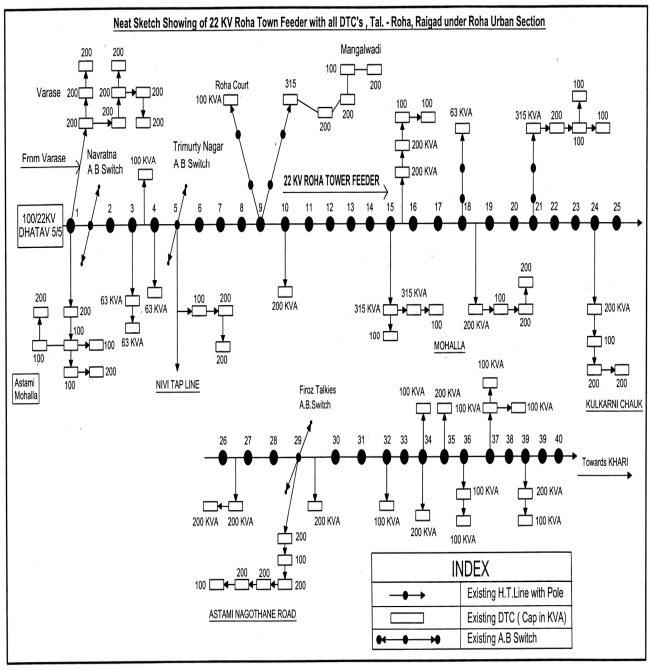

Fig.2. Single line diagram of the Roha town feeder.

Fig.3. Relay and the terminal block picture of Roha town feeder.

Fig. 4 shows the data collection in Excel file with all the parameters noted down on a time basis.

SR NO	DATE	TIME		DURATION	REASON	AFTER TRIPPING						BEFORE TRIPPING						PROTECTION
		FROM	TO			V	R	Y	B	E	F	TIME	V	R	Y	B	E	F	P(MW)	(OPERTED)
1	01.03.2015	1.25	1.30	0.05	EF	0.00	00.25	01.21	00.30	01.05	0.00	1.00	24.3	46				49.98	1.74	EF TRIP
												2.00	24.4	46				50.14	1.74	
2	01.03.2015	4.12	4.17	0.05	EF	0.00	00.11	00.10	01.91	01.85	0.00	4.00	24.7	46				50.28	1.74	EF TRIP
												5.00	24.9	03				50.23	0.11	
3	01.03.2015	4.17	4.30	0.13	EF	0.00	00.49	00.84	02.16	01.85	0.00	4.00	24.7	46				50.28	1.74	EF TRIP
												5.00	24.9	03				50.23	0.11	
4	01.03.2015	4.30	4.35	0.05	EF	0.00	00.47	00.75	02.02	01.93	0.00	4.00	24.7	46				50.28	1.74	EF TRIP
												5.00	24.9	03				50.23	0.11	
5	01.03.2015	6.35	6.40	0.05	EF	0.00	00.15	00.16	02.05	01.95	0.00	6.00	24.7	03				50.18	0.11	EF TRIP
												7.00	24.6	04				50.06	0.15	
6	01.03.2015	7.25	7.30	0.05	EF	0.00	00.13	00.16	02.01	01.93	0.00	7.00	24.6	04				50.06	0.15	EF TRIP
												8.00	24.4	04				50.07	0.15	
7	01.03.2015	9.30	9.35	0.05	RY	0.00	01.53	01.79	00.02	02.71	0.00	9.00	24.1	04				50.02	0.15	RY TRIP

Fig.4. Excel sheet of monthly data collected.

Table 1

Notations used in Fig.4

Parameter	Notation
V	22 kV Voltage
R	R Phase Current
Y	Y Phase Current
B	B Phase Current
E	Ground Current
F	System Frequency
P	Power

Fault statistics and analysis

There are lots of possibilities for generation of faults in the overhead transmission lines and the distribution lines. Some of the studied faults are as follows

- L to G - Single line to ground faults
- L to L - Line to line faults
- 2L to G - Double line to ground faults

Table 2 and Fig. 5 illustrate the type of faults and their respective numbers in the year 2014. It could be clearly seen that the Line to ground faults are dominating in comparison with other faults. The Line to ground faults are 82.63% of the faults throughout the year.

Table 2

Type and number of faults in the year 2014

Type of Faults	Number of Faults in 2014
L to G	238
L to L	42
2L to G	6
LLL	2
LLLG	0
Shutdowns	81

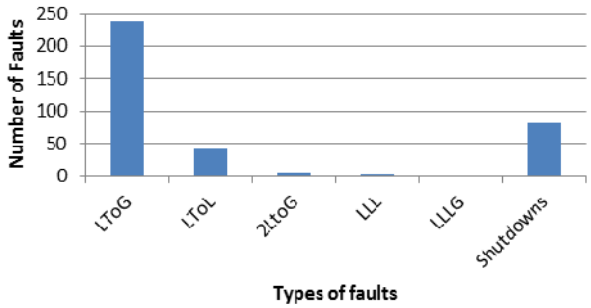

Fig.5. Number of faults occurred in the year 2014 in Roha town feeder.

Table 3 and Fig. 6 illustrate the type of faults and their respective numbers in the year 2015. It could be clearly seen that the Line to ground faults are the major part of the faults. The Line to ground faults are 84.68% of the total faults throughout the year.

Table 3

Type and number of faults in the year 2015

Type of Faults	Number of Faults in 2015
L to G	271
L to L	38
2L to G	11
LLL	0
LLLG	0
Shutdowns	54

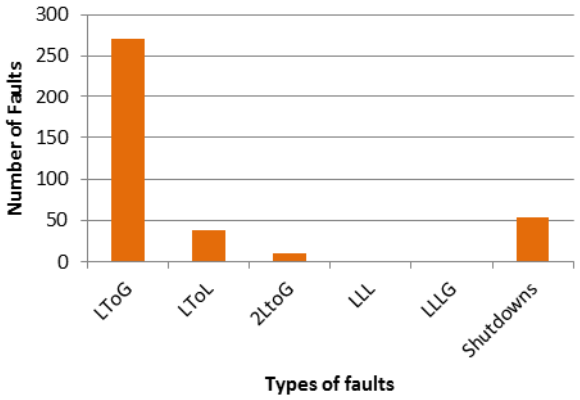

Fig.6. Number of faults in the year 2015 in the Roha town feeder.

Table 4 and Fig. 7 illustrate the type of faults and their respective numbers in the year 2016. It could be seen that the Line to ground faults are again dominating. The Line to ground faults form 76.82% of the total faults throughout the year.

Table 4

Type and number of faults in the year 2016

Type of Faults	Number of Faults in 2016
L to G	252
L to L	62
2L to G	13
LLL	0
LLLG	1
Shutdowns	56

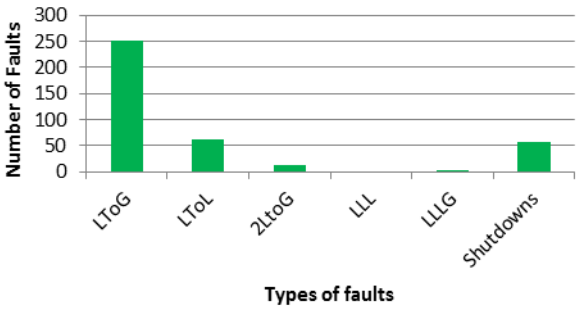

Fig.7. Number of faults in the year of 2016 in the Roha town feeder.

The complete data analysis for the three years of Roha feeder is done and some of the core points of analysis are as follows:

- Most of the faults of 2014 are due to the L to G i.e. single line to ground fault. From Figure 5, it could be seen that around 240 L to G faults have occurred, which is more than 80% of the total faults for the year 2014.
- A similar conclusion could be drawn for the years 2015 and 2016. It is clearly seen from Figure 7 that the single line faults are approximately around 250, which is a significant number.
- The second most frequent fault is line to line fault with an average of 15% for the three years.
- Double line to ground faults cover about 3% of the total faults. The faults of the two other types have occurred very rarely.

Observations on the cause of the faults and future work

The above data indicates the actual situation of electrical power distribution system in India. Because of the large geographical area and length of distribution network, the maintenance becomes difficult. The enormous growth of distribution system due to continuously increasing pressure on the Utilities Company for issuing more agricultural connections cannot be accurately predicted. Medium voltage lines as well as Low voltage lines are subject to faults even due to animal accidents because of bare conductors. The tree growth also paves such large number of faults. The distribution transformers cater to the requirement of a large area. The possibility of occurrence of faults increases. The natural diversity is also very large and probably system has to be designed considering local conditions.

In day-to-day time, the situation of the faults occurs in various forms. Different cases have been illustrated in Fig. 8. The breakdown of insulation also found at many places. The insulation breakdown can be avoided with the help of precaution by predetection of insulation fault techniques. There is a need to do better plan from maintenance point of view. Identification of cause of faults like wind speed or climatic conditions, look for non-permanent fault, visible burns and vegetation contacts. The fault analysis method gives a better identification of the exact reason.

Loose connection [8] - Fig. 8(a, b) - due to faulty 22kV disc and pin insulators in distribution lines can also be a cause of faults. Fig. 8 (d) shows fall of tree branches on lines.

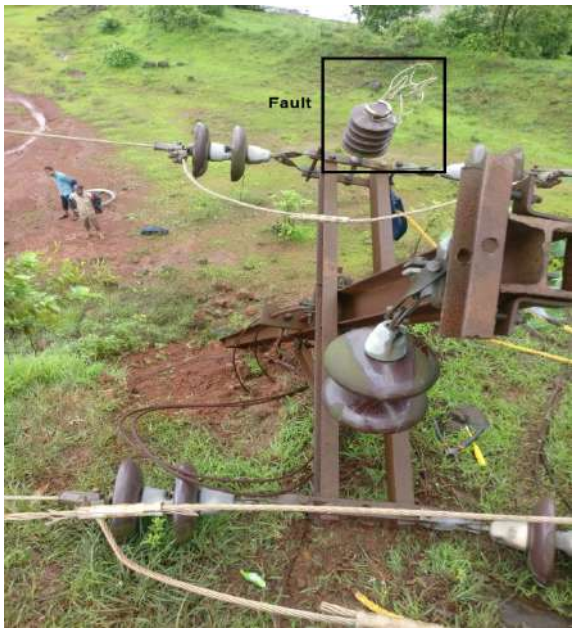

(a)

(b)

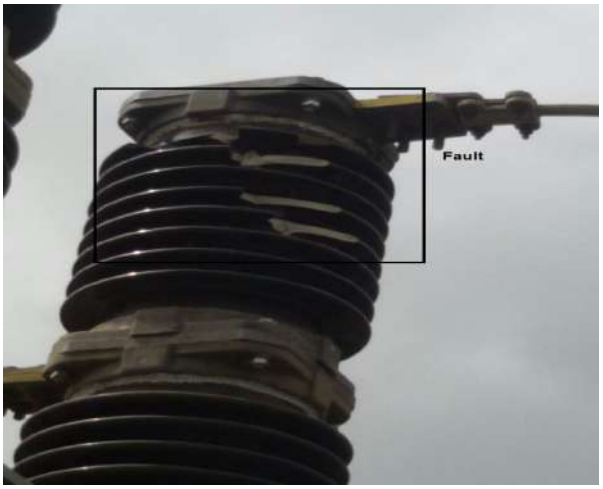

(c)

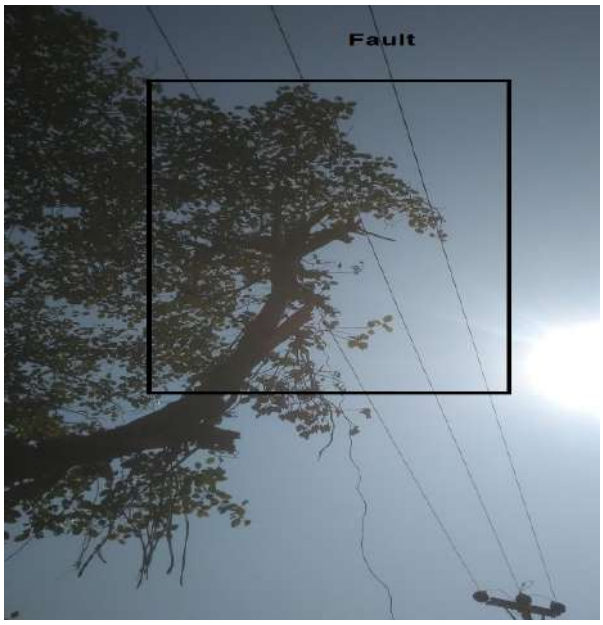

(d)

(e)

(f)

Fig.8. Real time fault condition situations at different places.

The fault cause recognition technique is important for fault detection purpose. It involves finding out the possible fault cause with help of data record for the last three years, whether it is in 1-phase, 2-phase and/or 3-phase lines. Also, what is the fault duration, whether it is repeated fault or not, as well as, further power arc length investigation. Cause of the fault also occurrs, if heavy rain-fall in presence of wind force due to heavy wind speed, this can lead to fault shown in Fig. 8 (f).

More reasons for the fault occurrence have been shown in Fig. 9. It shows accidental incidences due to environmental sudden change (Fig. 9 (a) and (b)). Fig. 9 (c) also shows a conductor snapping due to flood.

(a)

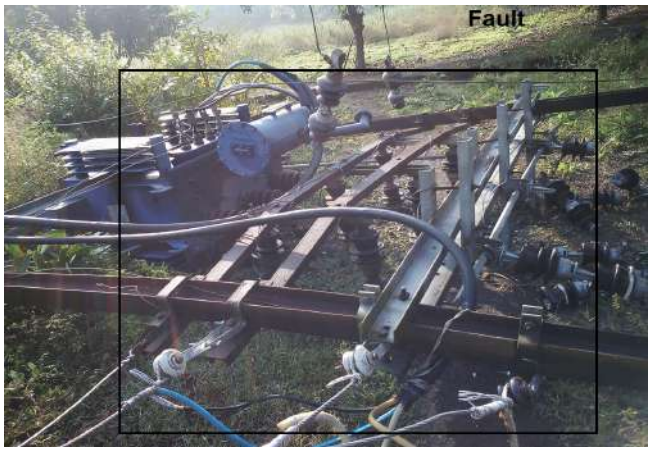

(b)

(c)

Fig. 9. More reasons for fault occurrence.

We propose to create a simulation model of this grid in Matlab to study occurrences of faults. To reduce the number of faults in our system, we use reclosers for interrupting overloads but not actual faults. It allows temporary faults to be recovered so that the grid is restored quickly, but at the time of major faults the system disconnects. Ten years back, the system used reclosers, which was not successful due to communication problems. For future work we will divide the 22kV feeder into different sections or zones, which will help to automatically isolate a section when fault occurs in the line. It senses value of current above its rated current and then de-energizes using reclosers. Renewable energy sources such as photovoltaic, biomass, wind power, micro turbine can be used independently at the time of faults (interrupted time).

Conclusion

The distribution of the faults for the considered three-year period is as follows: L to G-81.30%, L to L - 15.17%, 2L to G is 3.20%, LLL - 0.22%, LLL to G is 0.12%.The existing tools for fault localization do not allow its fast detection and usually faults lead to unnecessary long breakdowns. On the basis of the chosen mathematical models, a Matlab Simulink model will be created which will allow simulation of already registered faults, as well as the implementation of impedance trajectory method for fault localization. On the basis of this model, optimization technique will be employed and wireless sensor network will be introduced. This will allow minimizing the breakdown time.

Acknowledgement

The authors gratefully acknowledge the help and support from local utility company MSEDCL, Roha (Maharashtra state electricity distribution company Ltd.) during the field visit in their distribution network and Data of faults from substation of MSETCL (Maharashtra state electricity transmission company Ltd.).

REFERENCES

[1] Teng Jen-Hao. Systematic short circuit analysis method for unbalanced distribution systems. IEE Proc. Generation, Transm., Distribut., Vol. 152, No. 4, 2005, pp. 549–555.

[2] Paz, M.C.R., R.G. Ferraz, A.S. Bretas. System unbalance and fault impedance effect on faulted distribution networks. Computers and Mathematics with Applications, vol. 60, 2010, pp. 1105–1114.

[3] Halpin, S.M., L.L. Grigsby, C.A. Gross, R.M. Nelms. An improved fault analysis algorithm for unbalanced multi-phase power distribution systems. IEEE Trans. Power Deliv., Vol. 9, No. 3. 1994, pp. 1332–1340.

[4] Ibe, A.O., B.J. Cory. A travelling wave-based fault locator for two- and three-terminal networks. IEEE Trans. Power Deliv., Vol. 1, No. 2, 1986, pp. 283- 288.

[5] Ranjbar, A.M., A.R. Shirani, A.F. Fathi. A new approach for fault location problem on power lines. IEEE Trans. Power Deliv., Vol. 7, No. 1, 1992, pp. 146- 151.

[6] Johns, A.T., P. Aganval. A new approach to power line protection based upon the detection of fault induced high frequency signals. IEE Proceedings, Vol. 137, Pt. C, No. 4, 1990, pp. 307-313.

[7] Filomena, A.D., M. Resener, R.H. Salim, A.S. Bretas. Distribution systems fault analysis considering fault resistance estimation. Electrical Power and Energy Systems, Vol. 33, 2011, pp. 1326–1335.

[8] Mueller, D., J. Lamoree. Detecting, identifying, and correcting power quality problems. Power Quality'98 / Power Value'98 Proceedings,1998, pp. 221-228.

Eng. Vikas Gaikwad *- graduated from Govt .Engineering college Karad in Shivaji University in 1993 and completed his Master degree (M.E.) in 2000 at VJTI, Mumbai University, India, in Control Systems. Currently he is pursuing PhD in Dept. of Electrical Power Engineering, Technical University of Sofia , Bulgaria. Vikas has more than 5 years teaching and 17 years industrial experience in the field of electrical distribution. From 1994 to 1999 he was Lecturer and Since 1999 he has been working as Junior Engineer to Executive Engineer in MSEDCL, one of the leading Utility companies in Maharashtra. His main fields of scientific interest and expertise are in the area of Electrical Power Distribution.*

tel.: 9833968431 e-mail: vvg1771@gmail.com.

Received on: 07.02.2018

Some features and opportunities for calibration of analyzers of electric power by total harmonic distortion

Plamen Tzvetkov, Krasimir Galabov, Ivan Kodjabashev

The possibility for evaluation of the quality of electrical energy for the purpose of calibration of analyzers is considered by using a periodic square-wave pulse signal instead of the traditionally used harmonic signals. The square-wave pulse signal is represented in Fourier series, as each harmonic component is a function of the amplitude and the impulse signal duty ratio. A metrological analysis of the correction of the generated by the standard calibrator values of total harmonic distortion has been performed.

Keywords – analyzer of electric power, calibration, total harmonic distortion.

Някои особености и възможности при калибриране на анализатори на електрическа енергия по коефициент на нелинейни изкривявания (Пламен М. Цветков, Красимир С. Гълъбов, Иван Н. Коджабашев). *За целите на калибрирането на анализатори за оценка на качеството на електрическата енергия се разглежда възможността да се използва периодичен правоъгълен импулсен сигнал вместо традиционно използваните хармонични сигнали. Правоъгълният импулсен сигнал се представя в ред на Фурие, като всяка негова хармонична съставка се явява функция на амплитудата и коефициента на запълване на импулсния сигнал. Направен е метрологичен анализ на поправката на генерираните от еталонния калибратор стойности на коефициента на нелинейни изкривявания*

Ключови думи: анализатор на електрическа енергия, калибриране, коефициента на нелинейни изкривявания.

Introduction

Electricity analyzers are the measurement devices that provide an adequate assessment of the quality of the electrical energy. These measuring instruments measure the values of more than ten electrical quantities and parameters of the electrical energy, process the collected measurement information and provide a quality estimate according to the established normative basis.

The development of the technique and technology in economies, related to the creation and use of devices and facilities, sensitive to the described disturbances of the electricity network, requires adequate maintenance and traceability of the metrological characteristics of the power analyzers. This is achieved by calibrating of these devices with respect to the relevant quantities and parameters.

Calibration by total harmonics distortion (THD) and mathematical model

In calibrating of the electrical energy analyzer, referred further as the analyzer, the method of comparison of the measuring instrument with the traceable standard (reference calibrator, shortly - a calibrator), corresponding to the requirements of the traceability chain, according to the block diagram of Fig.1 is applied.

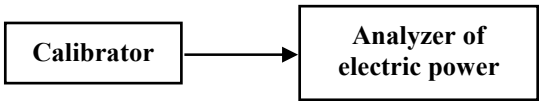

Fig.1. Scheme of calibration.

The calibration process determines the actual values of the corresponding total harmonic distortion of voltage or current. In the calibration the relationship between the reading of the analyzer and the realized by the calibrator total harmonic distortion voltage or current is established.

The mathematical model for the estimate of the actual effective value of the voltage THD, according to [1] is the following:

(1) $$THD_{U,act} = THD_{U,cal} - \delta THD_{U,et} + \delta THD_{U,res.cal} \ ,$$

where:

- $THD_{U,cal}$ - is the measured effective value of the THD voltage obtained by the calibrated analyzer, using in repeated measurements the estimate $THD_{U,cal} = \frac{1}{k}\sum_{i=1}^{k} THD_{U,cal,i}$, determined as an average value of the individual observations (measurements) $U_{n,cal,i}$

- k - is the number of measurements usually selected $k \geq 10$
- i - is the measurement index
- $\delta THD_{U,res.cal}$ - is the correction of the measured value of the THD voltage, due to the resolution of the calibrated analyzer

  $\delta THD_{U,et}$ - is the correction of the set by the calibrator harmonic voltage, which is generally due to different reasons such as:

– $\delta THD_{U,s.et}$ - a deviation of the set (generated) value of the calibrator due to combined effects by offsets, non-linearity, and other instrumental and methodic imperfections of the calibrator. This deviation can be determined from the calibrator technical documentation (while the calibrator is not calibrated) or from its calibration certificate as a correction of the calibration point ;

– $\delta THD_{U,dr.et}$ - a drift of the generated by the calibrator value, compared to the calibrator's last calibration (a drift since its last calibration)

– $\delta THD_{U,t.et}$ - a deviation of the calibrator value as a result from a change in the environment temperature;

– $\delta THD_{U,l.et}$ - a deviation of the calibrator value due to changes in the supply voltage;

– $\delta THD_{U,z.et}$ - a deviation of the calibrator as a result from the energy exchange of the calibrator due to the input impedance of the calibrated analyzer.

In calibration of a particular analyzer only these components should be considered which have the most significant contribution to the correction $\delta THD_{U,et}$.

The deviation of the calibrator set point value of the total harmonic distortion by voltage of the calibrator $\delta THD_{U,s.et}$ is determined by the relationship

(2) $$\delta THD_{U,s.et} = \delta_{THDu,et} THD_U,$$

where:

- THD_U is the effective value of the THD by voltage set by the calibrator,
- $\delta_{THDu,et}$ is the relative error of the calibrator.

Similarly, the mathematical model for estimating of the actual effective value current total harmonic distortion according to [1] has the form:

(3) $$THD_{I,act} = THD_{I,cal} - \delta THD_{I,et} + \delta THD_{I,res.cal},$$

where the individual components for the harmonic currents in the expression are analogous to the components of THD voltages in (1).

In calibration of the analyzer using a voltage THD by the help of the calibrator, the nominal effective voltage value of the main (first) harmonic $U_{1nom} = 230V$ and an effective value for the corresponding (relevant) total harmonic distortion, for which the analyzer is calibrated, are set. This approach can be applied only if the calibrator has the ability to generate a periodic signal, which is the sum of two or more harmonic signals, one of which is the voltage of the main (first) harmonic with a frequency $f = 50Hz$. If the calibrator does not have such a possibility, in the calibration of the analyzer it is suggested to use a periodic squarewave bipolar signal.

The calibration of the analyzer of the electric power based on a current total harmonic distortion is analogous to the calibration of voltage THD. The only difference is the use of relationship (3) instead of (1), therefore, the present paper considers only the process, the features and the possibilities for calibration of the total harmonic distortions by voltage.

Calibration of total harmonic distortion using a periodic squarewave bipolar signal

The periodic squarewave pulse signal is one of the most common reference signals. In Figure 2 the shape of a periodic squarewave bipolar pulse signal (voltage) $u(t)$ is shown.

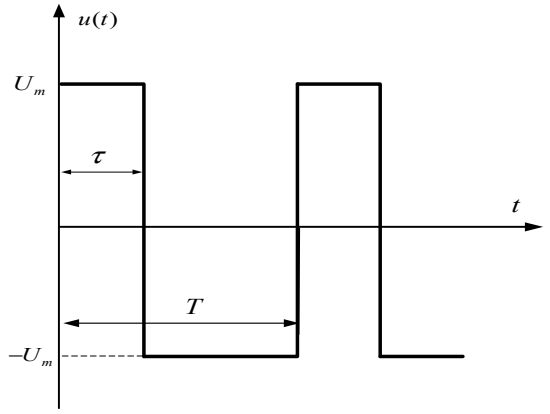

Fig.2. Timing diagram of periodic bipolar squarewave signal.

It is described by the expression:

(4) $$u(t) = \begin{cases} +U_m & t \in 0, \tau \\ -U_m & t \in \tau, T \end{cases}$$

where:

- U_m is the amplitude of the impulse,
- τ - is the duration of impulse,

- T - is the period of the pulse signal

An important parameter of the periodic pulse signal is its duty cycle μ, which depends on the duration of the impulse and the period of the pulse signal and is determined by the expression $\mu = \frac{\tau}{T}$.

By applying the decomposition of the periodic bipolar squarewave signal in Fourier series [2], [3] according to (4), the following expression is obtained:

$$x(t) = 2U_m(\mu - 0{,}5) + \frac{4U_m}{\pi}\sum_{n=1}^{\infty}\frac{\sin(n\pi\mu)}{n}\cos\left(\frac{2n\pi t}{T}\right), \quad (5)$$

and the total harmonic distortion according to [4] is the following:

$$THD_U = \sqrt{\frac{\mu(1-\mu)\pi^2}{2\sin^2(\pi\mu)} - 1}\ , \text{ за } 0 < \mu < 1, \quad (6)$$

From equation (6) it is seen that the only parameter, which affects the coefficient of non-linear distortion of the spectrum of the periodic squarewave pulse signal is its duty cycle μ. Graphically this relation is represented in Figure 3. Thus, for calibrating the analyzer by total harmonic distortion values for the duty cycle μ can be set.

Analysis of error in calibration using total harmonic distortions by voltage, through setting duty cycle by periodic squarewave pulse signal

In this case, it is interesting to study the influence of the error with which a duty cycle is set μ on the error setting of the total harmonic distortion THD. To determine this influence it is necessary to find the sensitivity using equation (6). By definition it is

$$S_{THDu} = \frac{dTHD_U}{d\mu}\ , \quad (7)$$

After differentiating (6) with respect to the variable μ the following expression is obtained

(8)

$$S_{THDu} = \frac{\frac{1}{2}\pi^2(1-\mu)\frac{1}{\sin^2(\pi\mu)} - \frac{1}{2}\pi^2\mu\frac{1}{\sin^2(\pi\mu)} - \pi^3(1-\mu)\mu\frac{\cos(\pi\mu)}{\sin^3(\pi\mu)}}{2\sqrt{\left[-1+\frac{1}{2}\pi^2(1-\mu)\mu\frac{1}{\sin^2(\pi\mu)}\right]}}$$

The relative error of the calibrator, determined from (7), is $dTHD_U = S_{THDu}d\mu$ and hence the relative error of the calibrator is

$$\delta_{THDu,et} = \frac{dTHD_U}{THD_U} = \frac{S_{THDu}}{THD_U}d\mu = \frac{S_{THDu}\mu}{THD_U}\delta_\mu = a_\mu\delta_\mu \quad (9)$$

where a_μ is the coefficient of influence of the relative error of the duty cycle μ.

In this case, it is interesting to study the influence factor function $a_\mu = a_\mu(\mu) = \frac{S_{THDu}\mu}{THD_U}$ for $0 < \mu < 1$, which is graphically represented in Fig. 4. It is seen that the range of the variation of the duty cycle $0 < \mu < 0{,}5$ ensures a smaller value of the relative error and it is preferable to range in $0{,}5 < \mu < 1$. This should be taken into account when realizing a value of the amplitude of a particular total harmonic distortion.

Using the expression (9) and the relationship (2) it is obtained

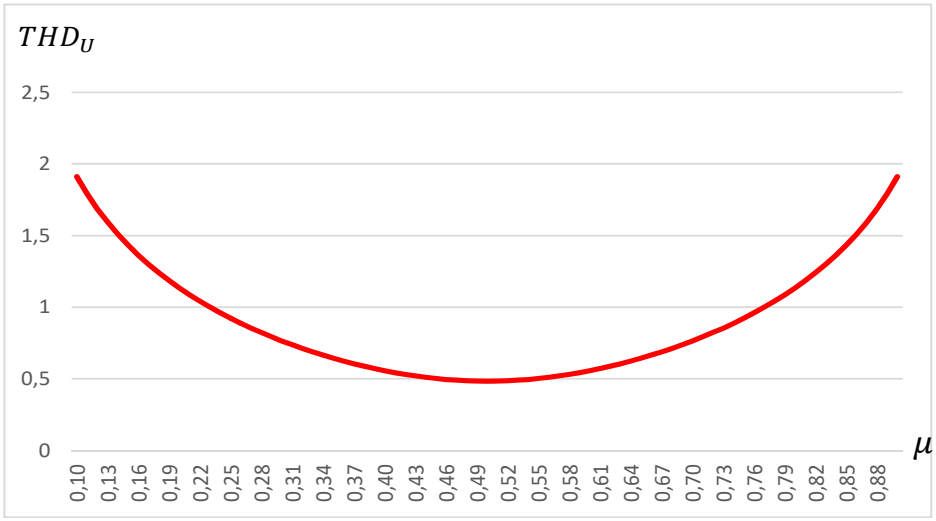

Fig.3. Graphical relation of $THD_U = f(\mu)$.

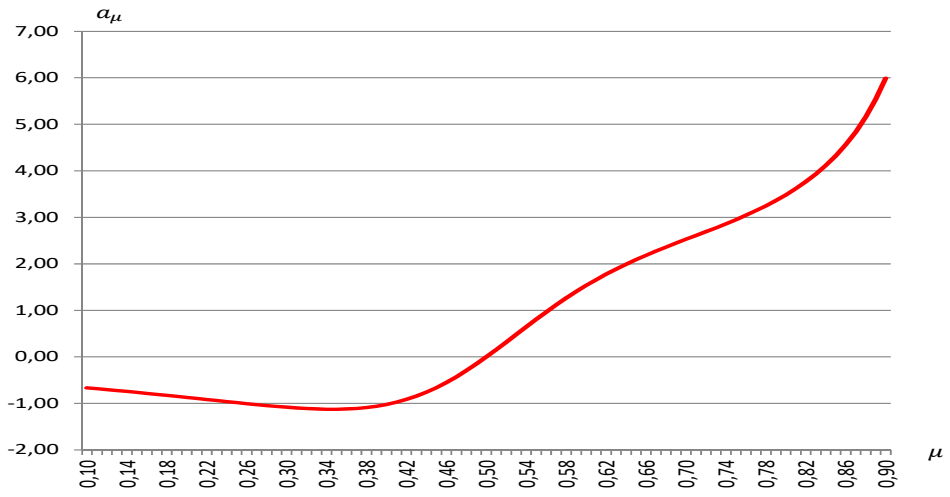

Fig.4. Graphical relation of $a_\mu = f(\mu)$

(10) $\delta THD_{U,s.et} = \delta_{THDu,et} THD_U = a_\mu \delta_\mu THD_U = S_{THDu} \mu \delta_\mu$

Conclusions

1. The method for calibration by THD using a periodic bipolar squarewave signal is appropriate when the reference calibrator cannot generate two or more THD signals.

2. The only parameter, which determines the error of setting the THD is the duty cycle μ.

3. The values of the harmonic voltages U_n including the main (first) harmonic U_1 do not affect the error of THD.

4. The values of the duty cycle μ should be in the range of 0 to 0,5 in order to ensure operation in the range of the smaller values of the influence factor a_μ of the relative error of the duty cycle.

5. The values of the amplitude of the squarewave impulse U_m and the duty cycle μ of the periodic bipolar squarewave signal should be chosen to ensure both: nominal value of the main harmonic and a specific value of THD for which the analyzer is calibrated. This is not always possible because the amplitude of the set periodic squarewave pulse signal is limited. Then these two parameters are chosen to realize the desired effective value of the THD at the greatest possible value of the main harmonic.

REFERENCES

[1] EA-4/02, Expressions of the Uncertainty of Measurements in Calibration (previously EALR2), 2013.

[2] Bronshtein, I.N., K. A. Semendyayev. Handbook of Mathematics, 3rd edition. Springer–Verlag, 1998.

[3] Korn, G.A., T.M. Korn. Mathematical Handbook for Scientists and Engineers. Definitions, Theorems, and Formulas for Reference and Review. McGraw–Hill, 1968.

[4] Blagouchine, I., E. Moreau. Analytic Method for the Computation of the Total Harmonic Distortion by the Cauchy Method of Residues. IEEE Transactions on Communications, vol. 59, no. 9, pp. 2478—2491, September 2011.

Prof. Dr. Plamen M. Tzvetkov *- MSc&Eng (1985) in Electrical Measurements, PhD (1998) in Metrology and Metrology Assurance, Professor (2012) in Electrical Measurements. Scientific field and interests: Electrical Measurements, Metrology and Metrology Assurance. Workplace: Technical University of Sofia, Department of Electrical Measurements at Faculty of Automatics. Address: Bulgaria, Sofia 1000, 8 Kliment Ohridski blvd, Web address: www.tu-sofia.bg.*

e-mail: tzvetkov@tu-soia.bg

MEng. Krasinir S. Galabov *MSc (2007) in the Department of Electrical Measurements, Faculty of Automatics, Technical University Sofia, Bulgaria. Scientific field and interests: Electrical Measurements, Metrology and Metrology Assurance, Virtual Instruments. Workplace: Technical University-Sofia, Faculty of Automatics, Department of Electrical Measurements, Address: Sofia 1000, 8 Kliment Ohridski blvd.*

e-mail address: k_galabov@tu-sofia.bg

Assoc. Prof. Dr. Ivan N. Kodjabashev *MSc (1969) in Electrical Measurements, PhD (1975) in Measurement Systems, Department of Electrical Measurements, Electrotechnical University (LETI) of Sankt Peterburg, Russia. Ass. Professor (1990). Scientific field and interests: Electrical Measurements, Metrology and Metrology Assurance. Workplace: Technical University-Sofia, Faculty of Automatics, Department of Electrical Measurements, Address: Sofia 1000, 8 Kliment Ohridski blvd.*

e-mail address: kodjabashev@tu-sofia.bg

Received on: 20.08.2018

Hysteresis loss analysis of magnetic materials with data acquisition system

Ivaylo Nedelchev

Magnetic materials are widespread in many fields of the electronics and electrical engineering. The most of them take place in the constructions of transformers, coil cores, electromagnets, measurement sensors etc. Thus, their parameters and characteristics are important to be studied precisely and within the whole operating range. Due to the nonlinear behavior of the characteristics of the magnetic materials it is crucial point to be obtained hysteresis parameters such, as saturation points and loss in the material. One advanced way to discover characteristics of the magnetic materials is usage of data acquisition system (DAQ). In this manner many tasks required precise and reliable solution can be executed. This paper represents the variant of the well-known oscilloscope's method via DAQ system. For obtaining hysteresis loop and programmable calculation of the loss the capabilities of the sampling of the DAQ measurement channels are used. With the software program, the instantaneous values of the studied voltages in real time are measured. The dynamic hysteresis cycle of the magnetization process is visualized.

Keywords – (data acquisition system, hysteresis loss, magnetic material).

Изследване загубите от хистерезис на магнитни материали чрез система за сбор на данни (Ивайло Й. Неделчев). *Магнитните материали са широко разпространени в много области на електрониката и електротехниката. Повечето от тях намират място в конструкциите на трансформатори, сърцевини на бобини, електромагнити, измервателни датчици и т.н. Важно е да се изследват точно в целия работен диапазон техните параметри и характеристики. Поради нелинейния характер на характеристиките на магнитните материали от голямо значение е намирането на параметрите на хистерезината крива: точки на насищане и загубите в материала. Подходящ съвременен метод за това е използването на система за сбор на данни (DAQ). По този начин могат да бъдат решени задачи изискващи точно и надеждно решение. Тази статия представя вариант на добре познатия осцилоскопен метод за изследване на загуби в магнитните материали чрез използването на DAQ система. За получаването на хистерезисната крива и софтуерното изчисление на загубите са използвани възможностите за дискретизация на входните канали за измерване на DAQ модула. Чрез програмата LabVIEW, в реално време се представят, както моментите стойности на измерените напрежения по време на процеса, така и изчислените загуби в материала.Визуализира се и динамичната хистерезисна крива.*

Introduction

In our practice and daily life, we use equipment, consisting magnetic materials. Every transformer, inductor, electromagnet, most of the sensors and medicine equipment include magnetic material in its construction. Due to the large usage in many fields of the practice, the magnetic materials parameters are important in the engineering science. Their main parameters and characteristics are frequency dependent and thus it is important to be studied within the whole operating frequency range. Due to the level of magnetization dependence of the magnetic materials, they manifest nonlinear behavior. Therefore it is crucial point to be obtained parameters such as saturation points and loss in the material [1], [2]. The effect of hysteresis during cyclically magnetization is a crucial reason for appearing the loss in materials [3] [4]. One advanced way to discover characteristics of the magnetic materials is usage of data acquisition system (DAQ). This paper represents one study over the hysteresis loss of the magnetic materials via DAQ

system. It is used the oscilloscope's method for obtaining hysteresis loop and also programmable calculation of the loss. The method can be applied for small by sizes parts of the tested magnetic materials, as well as for the big specimens with appropriate conditioning equipment - transducers and amplifiers. The program code based on LabVIEW software, calculates directly the loss in the material, using dynamic hysteresis loop. In real time instantaneous value of the studied voltages, as well as the hysteresis cycle of the dependence between magnetic flux density (*B*) and magnetic field strength (*H*) are measured and visualized.

Theoretical background of the method

In the oscilloscope's method the hysteresis curve of the magnetic material is obtained. The curve gives information for the hysteresis loss in the magnetic materials and for the main magnetic parameters such, as saturation points, retentivity and coercivity [1] [3] [5]. Fig. 1 shows the basic electrical diagram of the oscilloscope's method [1].

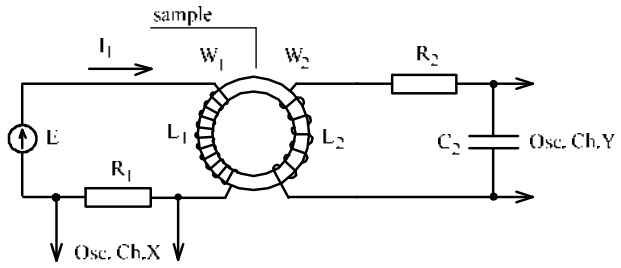

Fig.1. Electrical diagram of the oscilloscope's method.

In order to obtain hysteresis curve on the screen of the oscilloscope, it is necessary to have information for the magnetic flux density *B* and the magnetic field strength *H.* The magnetic quantities have to be connected with the electrical voltages, which could be measured easily with oscilloscope, adjusted to operate in XY mode. In order to work in sinusoidal magnetic flux density regime, the next condition has to be fulfilled: $R_1 << \omega L_1$ [1].

On the X channel of the oscilloscope voltage u_x is applied, which is in relation of the magnetization current i_1. According the Ampere's law (1) magnetic field strength *H* depends on the magnetization current i_1.

$$H_t.l_{AV} = w_1.i_1, \quad (1)$$

where H_t is the instantaneous value of the magnetic field strength, l_{AV}, is the average length of the magnetic line into the specimen's core, w_1 is the number of the turns in the primary coil.

Using the Ohm law, magnetization current can be represented as a drop of the voltage on the known resistance (R_1). Thus, the applied voltage on the X plates of the oscilloscope is measured as the drop of the voltage on the resistance R_1 (u_{R1}) in the primary circuit of the experimental set. In this manner it could be made relation with the magnetic field strength instantaneous value H_t.

$$u_x = u_{R1} = R_1.i_1 = \frac{R_1.l_{AV}}{w_1}.H_t . \quad (2)$$

The voltage applied on the Y plates of the oscilloscope is obtained after integration circuit, formed with the resistor R_2 and capacitor C_2 and can be expressed as:

$$u_y = u_{C2} = \frac{1}{C_2}.\int i_2 dt , \quad (3)$$

where i_2 is the current in the secondary circuit, C_2 is the capacity of the integration unit. According the KVL, the electromotive voltage in the secondary coil is [2] [3]:

$$e_2 = -w_2.S.\frac{dB_t}{dt} = i_2.R_2 + L_2.\frac{di_2}{dt} + \frac{1}{C_2}.\int i_2 dt , \quad (4)$$

where *S* is the cross section of the core, w_2 is the number of the turns of the secondary coil, B_t is the instantaneous value of the magnetic flux density, L_2 is the inductance of the secondary coil.

The components of the secondary circuit are chosen to be with the following relations:

$$R_2 >> \omega.L_2 , R_2 >> \frac{1}{\omega.C_2} ,$$

where ω is the angular frequency. Thus, the expression (4) can be written as:

$$e_2 = -w_2.S.\frac{dB_t}{dt} \approx i_2.R_2 . \quad (5)$$

According expressions from (3) to (5) can be found the drop of the voltage on the capacitor C_2 – u_{C2} and respectively voltage u_y is:

$$u_y = u_{C2} = -\frac{w_2.S}{R_2.C_2}.B_t . \quad (6)$$

The scale of the obtained hysteresis curve depends on the constants (C_X and C_Y) of the X and Y channel of the oscilloscope [1]. Therefore, the scale coefficients (C_B and C_H) are:

(7) $$C_H = \frac{C_X . w_1}{R_1 . l_{AV}},$$

(8) $$C_B = \frac{C_Y . R_2 . C_2}{w_2 . S}.$$

It is known, that energy for cyclically magnetization of the specimen can be expressed as the contour integral by hysteresis closed curve, obtained by the oscilloscope's method. This integral is proportional of the area of the closed loop. The proportional coefficient depends on the scale coefficients (C_H and C_B), found in the equations (7) and (8) above. Then, the energy can be expressed as:

(9) $$E_H = \oint HdB = C_H . C_B . S_H,$$

where S_H is the hysteresis curve area. Therefore the specific hysteresis loss can be calculated as [1] [3]:

(10) $$P_H = \frac{f}{\rho} . E_H = \frac{C_H . C_B . f . S_H}{\rho},$$

where f is the magnetization current frequency, ρ = 7800 kg/m^3 is the volumetric mass density of the magnetic material. There is one more component of the specific loss in the magnetic materials – the Eddy current loss. The Eddy current loss can be expressed as [5]:

(11) $$P_E = \frac{\pi^2 . \sigma . f^2 . \tau^2 . B_{\max}^2}{6},$$

where σ = 2,174.10^6 S/m is electrical conductivity of the material, τ is the thickness of the plate, B_{max} is the amplitude of the magnetic flux density. For the experiment B_{max} < 0,3 T.

The total loss is sum of the Eddy current loss (11) and hysteresis loss (10). The calculation by the parameters above shows, that by frequencies in the span of 60 ÷ 140 Hz, for small thickness of the specimen's plate and low levels of magnetization, the Eddy current loss (P_E) can be neglected ($P_H >> P_E$).

Measurement equipment. Setting of the experiment

The main components of the study are: magnetic material specimen, DAQ system, software program.

Experimental specimen

For the magnetic material specimen, the core of the laminated cold-rolled electrical steel plates is used. The experiment is conducted with E - core shaped specimen with plate thickness (τ = 0,1 mm.). The physical dimensions of the core are shown on the Fig. 2. The main sizes are: a = 20 mm, b = 20 mm, c = 5 mm, d = 3 mm. The average length of the magnetic lines (l_{AV}), is assumed to be located in the middle of the magnetic branches of the E - core (dashed lines in Fig. 2). Then, according the sizes (a, b, c, d) given above, the total length path of the magnetic lines is: l_{AV} = 94 mm. and the cross section of the central branch is: $S = c.d$ = 30 mm^2. The windings of the coils have the following parameters: primary - w_1 = 1400 turns, secondary - w_2 = 1400 turns.

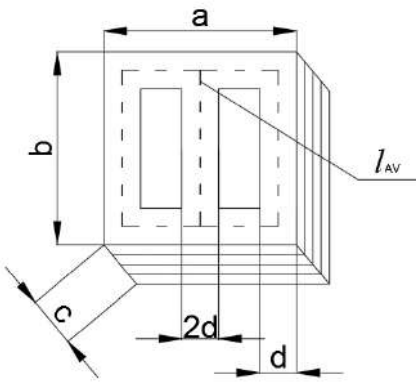

Fig.2. Shape and dimensions of the specimen.

DAQ system

For the experiments DAQ system model NI - 6211 of the National Instruments company is used. Data acquisition system type NI – 6211 contains 8 differential or 16 single ended analog inputs (AI), 2 analog outputs (AO), 4 digital inputs/outputs. The main parameters of NI – 6211 are [6]:

- Sampling rate (fs) 250 kS/s;
- Resolution 16 bits;
- Maximum working voltage for analog inputs (AI), Vi ±10 V.

The application of the DAQ system in the measurement method makes the experiment more precise in order to obtain clear dynamic hysteresis curve and simplify calculation of the scale coefficients (C_H and C_B) during the measurement. Their value is directly proportional to the measurement voltages received by the both input channels included in primary and secondary side of the experimental set. In this case, if the specimen has small sizes and experimental set doesn't need any transducers for measurement channels, C_X = 1, C_Y = 1 (in eq. (7) and (8)). This simplifies the calculation and increases the accuracy of the measurement during the dynamic changes of the specimen magnetization current. In other hand, the obtained results are with high resolution, due to the high sampling frequency rate (f_s = 10 kHz) of the measurement signals. They can be

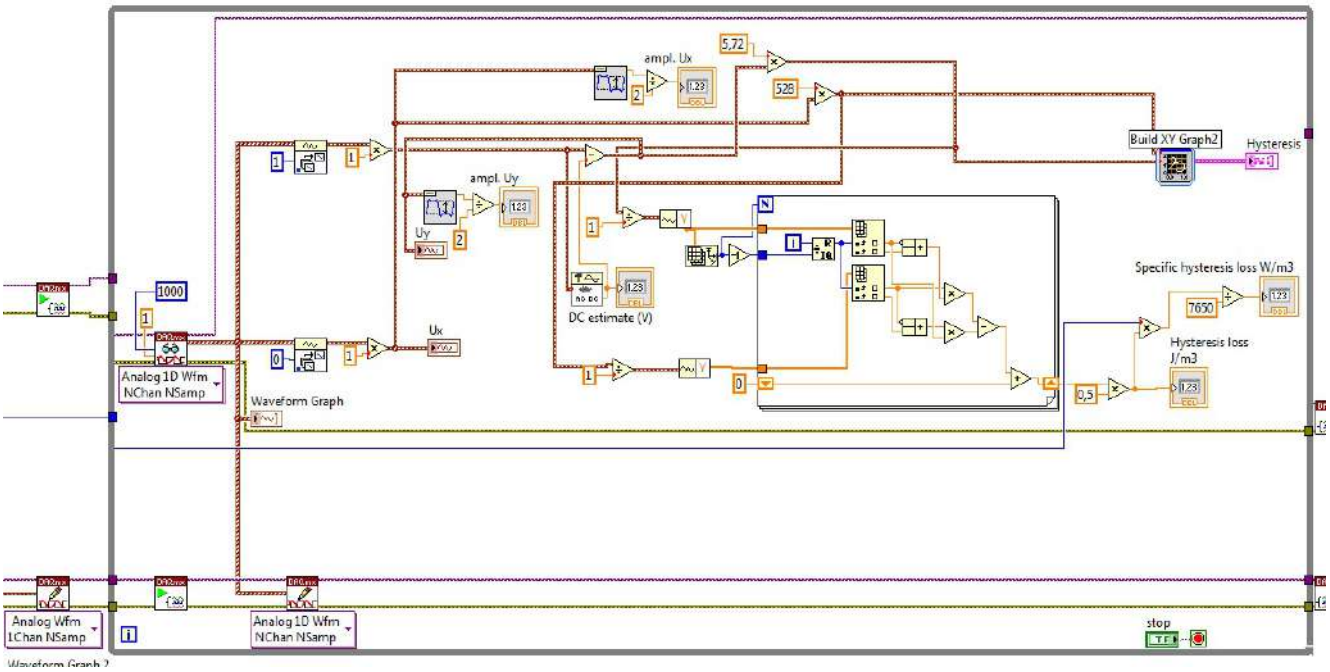

Fig.3.The part of the graphic code of the program.

represented in any form textual or graphical in real time. The hysteresis loss can be calculated and represented immediately during the measurement.

Software program

During the measurements, obtaining and calculation of the hysteresis curve, the LabVIEW software of the National Instruments company is used. It is a visual programming language, based on the graphically manipulating between program elements. The part of the graphic code is shown on the Fig. 3. The control panel of the program is shown in the paragraph of the obtained results, below.

Connection diagram of the experimental set

The inbuilt two analog output channels in NI - 6211 can generate signals with different types and shapes. For the experiment is used output AO 1, generating sinusoidal voltage, which peak to peak value vary between 1 - 10V depending on the magnetization of the specimen and the frequency of the magnetization is in the span of 60 ÷ 140 Hz. In the experiment are involved two input channels AI 1 and AI 4 for measurement the value of the magnetization current in primary coil and output voltage of the secondary coil. The used output and input channels of the NI – 6211, are adjusted to be in a differential mode [6]. The experimental electrical diagram is shown on the Fig. 4.

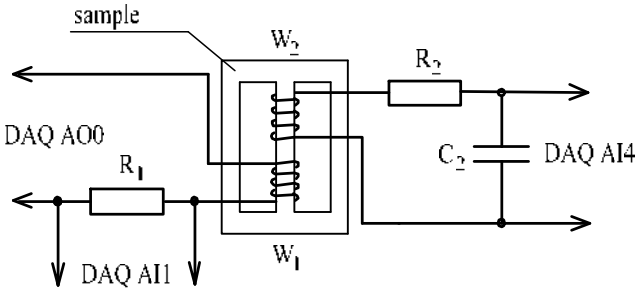

Fig.4. Electrical diagram of the measurement.

The nominal value of the electrical components are: capacitor C_2 = 100 nF, R_2 = 1,2 MΩ, R_1 = 52 Ω.

Estimation of the hysteresis loop area S_H

According (9) the energy for magnetization of the specimen E_H can be calculated by the area of the hysteresis loop S_H and scale coefficients C_B and C_H. One way for estimating the area S_H is to apply the Green's theorem [7]:

$$(12) \qquad \oint_H (u_x dx + u_y dy) = \iint_{S_H} \left(\frac{du_x}{dx} - \frac{du_y}{dy} \right) dxdy ,$$

where u_x and u_y are voltages which gives the area S_H if is fulfilled the following condition:

$$\frac{du_x}{dx} - \frac{du_y}{dy} = 1 .$$

Due to the sampling of the received voltage signals (u_x, u_y) with NI – 6211, the hysteresis loop can be represented as a polygon, consisting of n number of edges. The number n depends on the frequency sampling rate (f_s) of the measurement signals. Actually, the measurement data represent a multiplicity of points with Cartesian coordinates ($u_{x(i)}$, $u_{y(i)}$), which forms a two dimensional array. Then the Gauss's area formula (13) could be applied [7]. The expression (13) is a modification of the Green's theorem:

(13)

$$S_H = \left| \sum_{i=1}^{n-1} u_{x(i)}.u_{y(i+1)} + u_{x(n)}.u_{y(1)} - \sum_{i=1}^{n-1} u_{x(i+1)}.u_{y(i)} - u_{x(1)}.u_{y(n)} \right|,$$

where $u_{x(i)}$, $u_{y(i)}$, are the coordinates of the obtained curve, i.e. each sample of the measured voltages u_x and u_y.

Results

The magnetization of the specimen is conducted via output channel AO 1 of the NI – 6211. Maintained range of the output channel is ± 10 V. The control of the amplitude, form and frequency of the magnetization current is driven by software program. The program consists of control and connecting diagram panels. On the Fig. 5 is shown the control panel, which represents the manner of the driving measurements by supplying and receiving the voltages through the output (AO 1) and input (AI 1, AI 4) channels of the DAQ module. On the control panel the regulators for amplitude and frequency and the main diagram of the hysteresis curve are obvious, as well as the time-domain diagrams of the measured voltages in primary and secondary coil via analog channels AI 1and AI 4. On the top right position in the field of panel area are visible fields, which show calculation of the hysteresis loss by E_H and P_H in real time, obtained by Gauss's area expression (13).

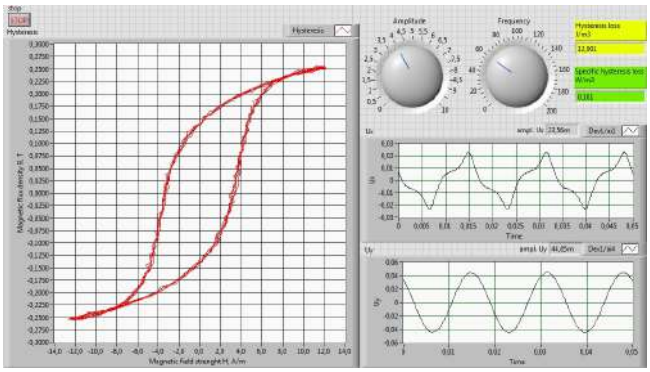

Fig.5.Control panel of the program.

For obtaining the magnetic parameters in broad operating span, the magnetization could be controlled by frequency and amplitude in order family of the characteristics to be built. For the experimental set, the output voltage frequency from AO 1, varies between 60 and 140 Hz, and its amplitude (by constant frequency) is changing in the range 3 V ÷ 10 V. Due to the real time graphical information and numeric representation of the main parameters of the measurement voltages, the experiment could be driven to the point of saturation, reaching the border hysteresis curve. This is visible either in the hysteresis curve diagram or in the time – domain diagram of the non – sinusoidal voltage u_x, which is related with the magnetic field strength H.

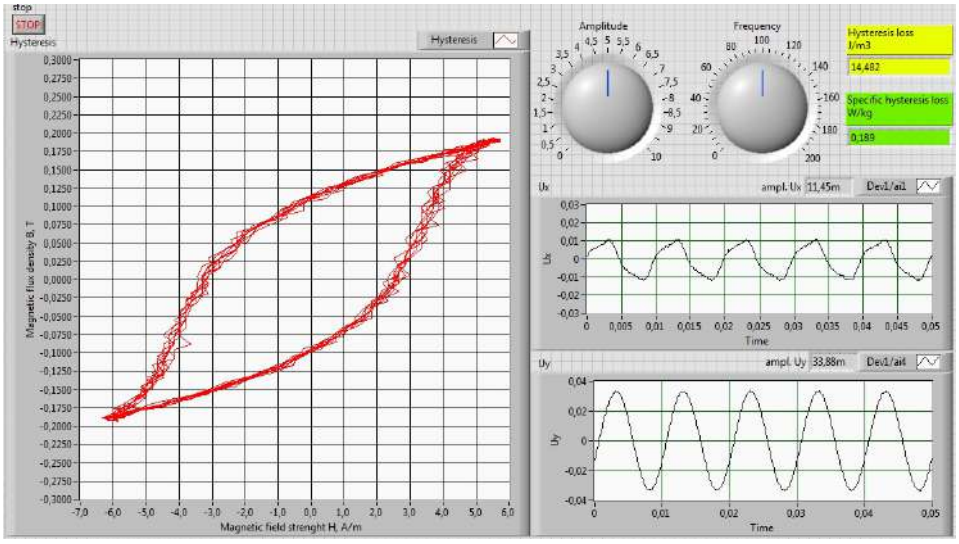

Fig.6. Control panel of the program by output voltage from channel AO 1 - U_{pp} = 5V, f = 100Hz.

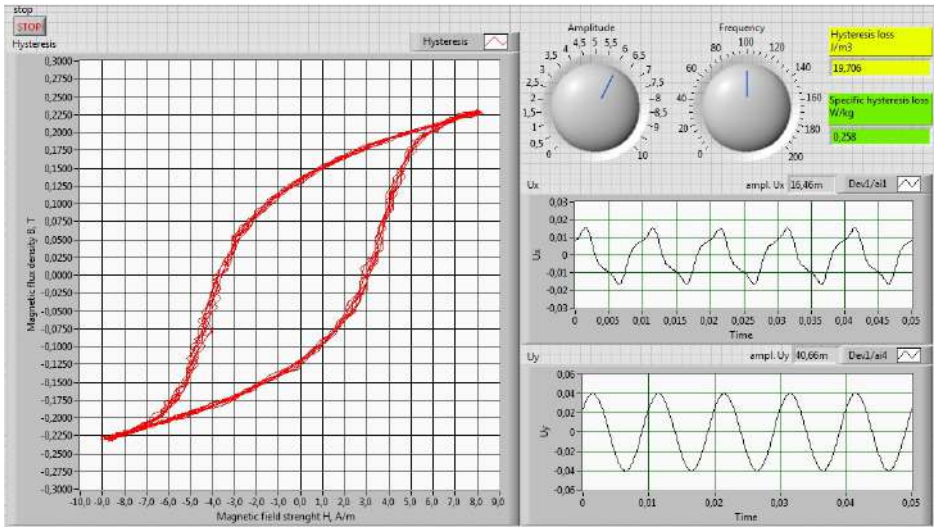

Fig.7. Control panel of the program by output voltage from channel AO 1 - U_{pp} = 6V, f = 100Hz.

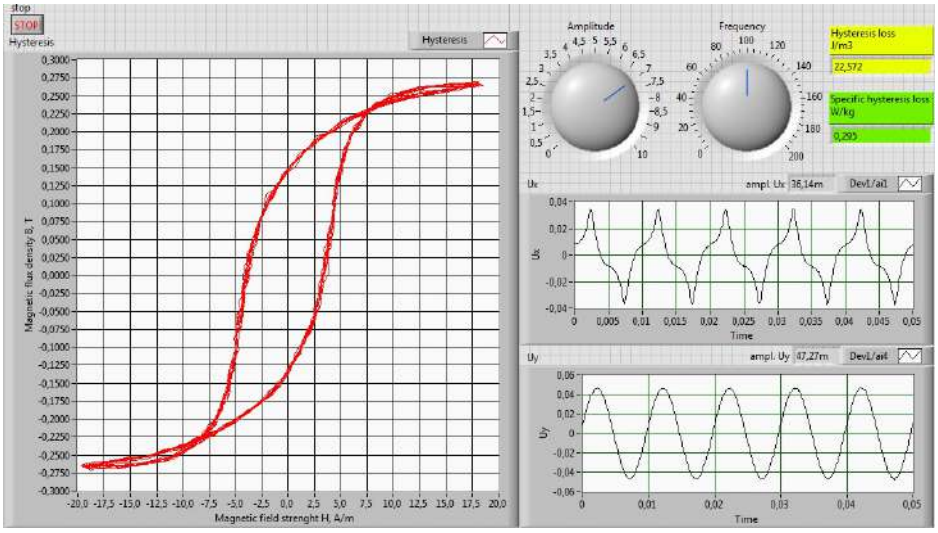

Fig.8. Control panel of the program by output voltage from channel AO 1 - U_{pp} = 7V, f = 100Hz.

On the Fig. 6 to Fig.8 the magnetization of the specimen are represented in the range of 5 V – 7 V for peak to peak value of the output voltage u_{pp} of the DAQ channel AO 1, by constant frequency $f_{const.}$ = 100 Hz. It is shown the corresponding drop of the voltages on the resistor R_1 in the primary circuit – u_x, as well as the inducted voltage in the secondary circuit - u_y.

The obtained graphical and numerical results show gradually increasing stages of the magnetization of the specimen. It is obvious (Fig. 6 to Fig. 8) that for magnetization current of 100 Hz, for this experimental set, is needed to supply voltage u_{pp} = 7 V in order to reach saturation level and border hysteresis curve.

This input voltage, causes a vast distortion level into the primary circuit (u_x), respectively on the magnetization current. The hysteresis closed curve is not clear shaped, due to the dynamical fluctuations during the cyclically magnetization. This causes alternating line borders of the curve during the time period, change its area and therefore the calculated hysteresis loss. In Table 1 data of the magnetization by frequency are represented in the range 60Hz – 140Hz of the magnetization input voltage u_{pp}. Increasing magnetization frequency, makes reaching the saturation level on higher values of the input voltage u_{pp}.

This is an effect of the increasing of the reactance in the primary circuit, which restricts the magnetization current. The trend in frequency domain is shown on the Fig. 9. Specific hysteresis loss P_H, is in dependence on the magnetization current, because of the enlarging the area of the curve S_H during the u_x and magnetization frequency f (eq. (10)). This is represented on the graphics in the Fig. 10.

Table 1

Hysteresis loss obtained by frequency range 60 – 140 Hz of the input magnetization voltage

$f_{const.}$	u_{pp}	u_x, amplitude value	u_y, amplitude value	E_H	P_H
Hz	V	mV	mV	J/m^3	W/kg
60	3	11,94	34,20	8,35	0,066
	4	23,56	44,85	12,91	0,101
	4,25	40,98	47,43	13,27	0,104
70	3	9,68	29,04	7,35	0,067
	4	14,20	38,40	12,02	0,112
	5	45,66	47,92	15,74	0,144
90	4	10,33	30,33	10,45	0,123
	5	13,55	37,59	15,76	0,185
	6,5	71,63	48,89	19,32	0,227
100	5	11,62	34,20	14,82	0,194
	6	16,13	40,82	20	0,261
	7	47,76	48,24	23,20	0,303
140	6	9,84	29,69	16,62	0,304
	8	14,52	39,20	27,43	0,502
	10	51,95	49,21	33,67	0,617

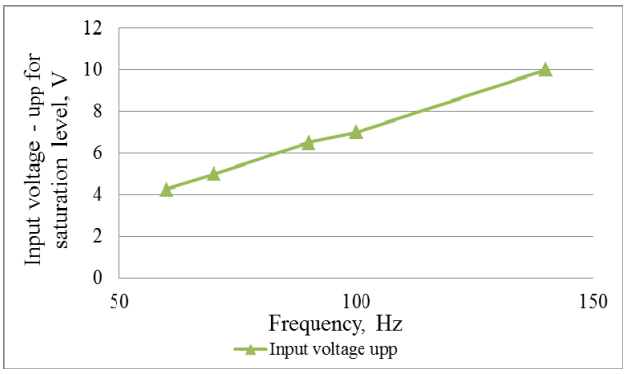

Fig.9. Needed Input voltage for reaching saturation level.

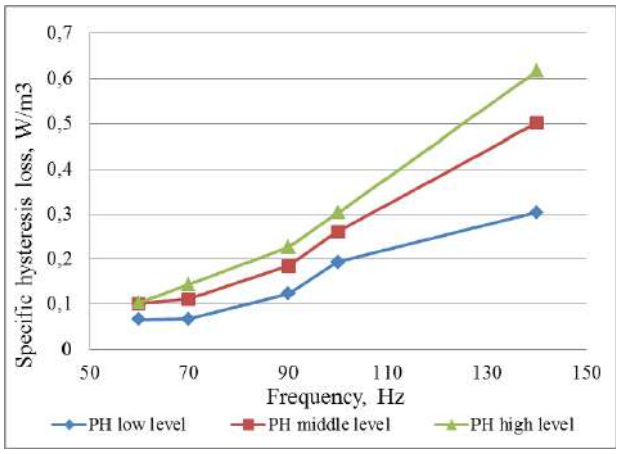

Fig.10. Specific hysteresis loss.

It has to be mentioned, that this manner of calculation of the hysteresis curve area is applicable below of the levels of saturation of the material. Above this level of the magnetization, the dynamic curve loop forms intersections and respectively the areas with the opposite sign in (13) are occurred. This makes the calculations not correct.

Conclusion

The experiment clearly shows one application of the DAQ systems in measurement the main parameters of the magnetic materials. DAQ system capabilities were applied upon the small magnetic specimens, which is one advantage of the experimental set. This could be done also for the specimens with bigger sizes, using appropriate amplifiers and transducers. With this basic experimental set, could be measured in real time a big number of the main parameters of the magnetic materials. This makes possible to be represented immediately the magnetization trends and characteristics such as hysteresis curve, primary magnetization curve, permeability during the magnetization and also to find the coercivity and retentivity. One crucial advantage over the oscilloscope's method, using DAQ in this type of measurements, is obtaining the dynamic hysteresis curve. The width of the curve borders shows the dynamic level of the process. Thus the fluctuations in the loss value can be estimated also. This could be observed during the low levels of magnetization. The involving of the DAQ system in the experiment increases the data accuracy and expands the measurement potential.

REFERENCES

[1] Matrakov, B. Electrical measurements. Sofia, Technica, 1989.

[2] Farhi, S., S. Papazov. Theoretical engineering. Sofia, Technica, 1987.

[3] Bertotti, G. Hysteresis in Magnetism. California, Academic Press, 1998.

[4] Parthasaradhy, P., S. Ranganayakulu. Hysteresis and eddy current losses of magnetic material by Epstein frame method-novel approach. The International Journal of Engineering and Sciencers, 2014, pp.85-93.

[5] Tumanski, S. Handbook of Magnetic Measurements. CRC Press, June 2011.

[6] http://www.ni.com/pdf/manuals/375195d.pdf

[7] http://mathworld.wolfram.com/PolygonArea.html

Assist. Prof. Ivaylo Nedelchev *assistant of electrical measurements in the Department of Theoretical engineering and Electrical measurements in Technical University of Varna.*

tel.:+359896666134 *e-mail: iynedelchev@abv.bg*

Received on: 29.05.2018

Overview of gyrator based G_m-C filters and their applications

Atanas Tanev

This paper reviews gyrator based G_m-C filters and their characteristics. The most common gyrator based G_m-C filter architecture is described. Different types of gyrator biquad are presented as well as the properties of simulated inductor in them are outlined. The circuit of fully differential OTA is considered and analyzed in more details. The key OTA parameters related to gyrator based G_m-C filters are presented. Moreover, different techniques for improvement the performance of OTAs is considered. This paper also includes a comparison between single stage and multiple stage OTA with respect to frequency dependence of G_m. Finally, gyrator based G_m-C filters applications for the frequency range starting from few Hz up to several hundred of MHz are summarized.

Keywords – G_m-C filter, gyrator, linearity enhancement, operational transconductance amplifier (OTA).

Обзор на G_m-C филтрите базирани на жиратор и тяхното приложение (Атанас Танев). *В този доклад е направен обзор на G_m-C филтрите базирани на жиратор и техните характеристики. Направено е описание на най-често използваната архитектура на G_m-C филтри базирани на жиратор. Презентирани са различните видове на жираторни звена от втори ред, като са посочени и основните свойства на симулираната бобина. Детайлно е разгледана и анализирана схема на напълно диференциална схема на ОТА. Презентирани са основните параметри на ОТА по отношение на G_m-C филтрите базирани на жиратори. Докладът също включва и сравнение между едностъпалните и многостъпалните по отношение на честотната зависимост на G_m. Накрая в доклада е направено обобщение на Gm-C филтрите базирани на жиратор за приложения от няколко Hz до няколкостотин MHz.*

Introduction

The necessity of integrated analog filters in very wide frequency range, makes G_m-C filters (also known as transconductance-C and OTA-C) very attractive [1], [2], [3], [4]. They have been intensively investigated for a long time now. The first articles appeared in mid-1960s.

Nowadays, G_m-C filters are still the most widely used type of analogue filters [2]. This is due to their excellent characteristics for IC design applications. Another advantage is the simple structures, which they are realized with. The basic element of the G_m-C filters is the operational transconductance amplifier (OTA).

Gyrator based G_m-C filters are commonly used at very low as well as very high frequency applications [2], [5]. The interest in this class of filters is constantly growing, which can be observed by the all new scientific results and practical implementations (Fig. 1). The data for the Fig.1 is obtained from IEEE Xplore database, the rise of papers in the last 15 years can be clearly seen.

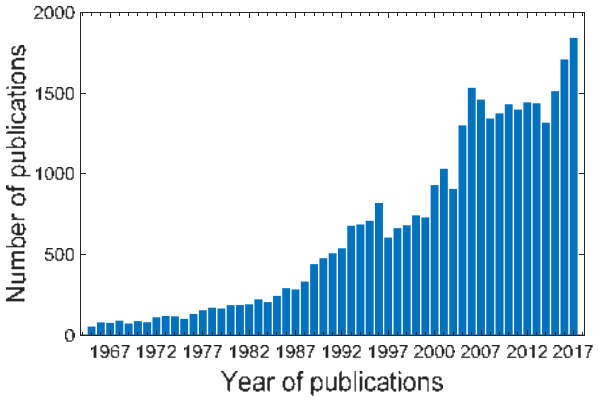

Fig. 1. Number of published articles in IEEE Xplore, related to G_m-C filters for the period 1965 – 2017.

This paper presents an overview of gyrator based *Gm-C* filters – common architecture, different types of biquad and properties of simulated inductor. The fully differential circuit of OTA is considered and analyzed. The key parameters of OTA related to G_m-*C* filters are outlined. Different techniques and approaches are proposed for improvement of the parameters of OTA. A comparison between single stage and multiple stage OTA with respect to frequency dependence is made pointing their strenghts and weakneess. The paper summarizes the applications for very low and frequencies as well high frequencies.

Gyrator based G_m-*C* filters

Gyrator filters are one of the most often used class of G_m-*C* filters. In general, these filters used a substitution method for direct replacement of grounded inductors in the *LC* ladder filters. The simulation of grounded inductors is done by placing single capacitive loads on the gyrator [1], [4], [6]. A circuit with two cascade-connected gyrators with a capacitor between them is used for the simulation of floating inductors in the *LC* ladder filters.

This substitution method allows to preserve the most important advantage of the *LC* ladder filter – the very low sensitivity with respect to component variation [1], [6]. These filters, however, are often designed by building gyrator biquads obtained by the corresponding *LC* circuits, as shown in Fig.2 [6], [7].

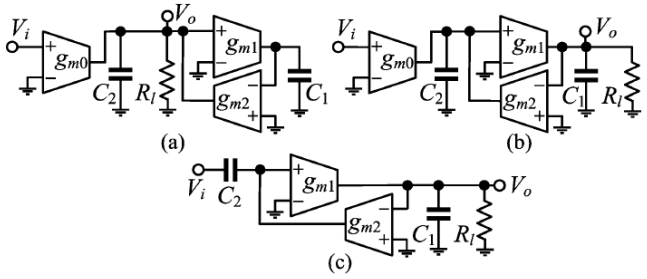

Fig.2. BP (a), LP (b) and HP (c) biquad based on gyrator tank.

There are not many architectures of gyrator filters and designers mainly work for the improvement of the amplifiers' performance. Tuning of the important filters parameters such as pole frequency and quality factor is made by changing the transconductance of OTAs and/or capacitors.

In order to obtain a good dynamic range of the gyrator based G_m-*C* filters, the following condition for identity must be fulfilled in all stages *[1]*

(1) $$\frac{g_{m1}}{C_1} = \frac{g_{m2}}{C_2}$$

In this way, the maxima of the voltages from both sides of the gyrator are obtained equal.

Properties of the simulated inductor

The circuit of a gyrator simulated inductor is shown in Fig.3(a). The parasitic input and output capacitances of OTA appear in parallel with capacitors C_1 and C_2; for this reason, they are considered as part of them. The OTAs in Fig. 3(a) have input resistances, which are assumed to be infinitely high, while their output resistances R_{o1} and R_{o2} are finite. The equivalent circuit of the simulated inductor is shown in Fig. 3(b).

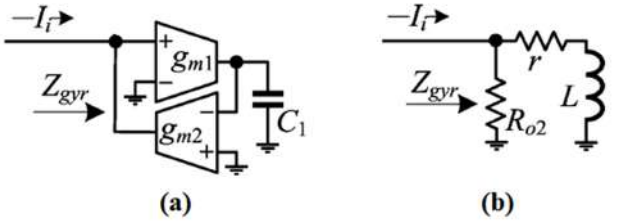

Fig. 3. (a) Circuit of simulated grounded inductor (b) its equivalent circuit

The elements of the simulated inductor are described by [1], [6]:

(2) $$L = \frac{C_1}{g_{m1}g_{m2}}; \quad r = \frac{1}{R_{o1}g_{m1}g_{m2}}$$

The quality factor of the simulated inductor for low frequencies is determined by the equivalent impedance of *L*, *r* and R_{o1}

(3) $$Z_{eq} = (j\omega L + r) \| R_{o2} = R_{eq} + j\omega L_{eq}$$

R_{eq} and L_{eq} are obtained from the following expressions

(4) $$R_{eq} = \frac{R_{o2}[r(R_{o2}+r)+\omega^2 L^2]}{(R_{o2}+r)^2+\omega^2 L^2}$$

(5) $$L_{eq} = \frac{LR_{o2}^2}{(R_{o2}+r)^2+\omega^2 L^2}$$

Fig. 4 shows the frequency dependence of R_{eq} and L_{eq}. From the figure it can be seen that when ω is small, R_{eq} is equal to $R_{o2}||r$, while when ω is large, R_{eq} tends to R_{o2}.

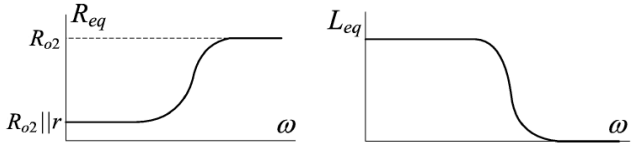

Fig.4. Frequency dependence of the equivalent L_{eq} and R_{eq}.

The ratio between ωL_{eq} and R_{eq} gives the Q factor of the equivalent inductor

(6) $$Q_L = \frac{\omega L R_{02}}{r(R_{02}+r)+\omega^2 L^2}.$$

Circuit description and analysis

After formulating the expressions for the pole frequency and the quality factor Q of the simulated inductor, we investigate the proposed OTA in [8], needed for realization the gyrator tank. Most often the OTA is based on differential amplifier stages as shown in Fig. 5.

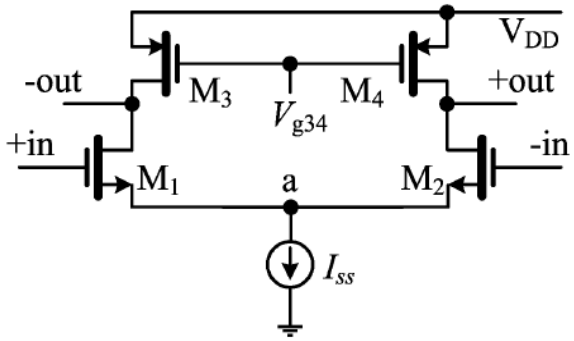

Fig.*5. Circuit of fully differential stage, used for realization of OTA.*

Transistors M_1 and M_2 are matched as well as transistors M_3 and M_4. The differential circuit of OTA from Fig. 5 consists of:

- Transistors M_1 and M_2 form the differential pair,
- DC current source I_{ss} providing the tail currents of the circuit,
- Transistors M_3 and M_4 representing the active load.

Usually, the current source I_{ss} is realized as a current mirror. The voltage V_{g34} on the gates of M_3 and M_4 is direct voltage (dc). By controlling V_{g34} the dc voltage of the terminals +out and –out of the outputs of the circuit are set.

In order to determine the G_m of the OTA amplifier an AC analysis of the circuit from Fig.5 should be done. For this reason, MOS transistors are substituted by their small-signal models. The small signal model of the OTA is shown in Fig. 6 [7].

The following equation for the current i_o is obtained:

(7) $$i_o = g_m \frac{v_{in}}{2}$$

where the transconductances g_m of the transistors are equal due to the matching of the transistors.

Therefore, the G_m of the amplifier is given by

(8) $$G_m = \frac{i_o}{v_{in}} = \frac{g_m}{2}.$$

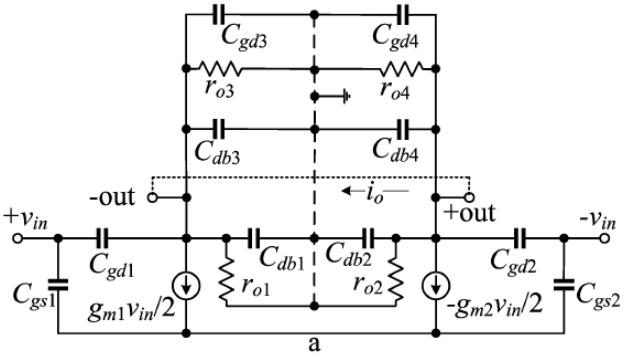

Fig.6. Small-signal model of the OTA from Fig. 5 [7].

One of the three available equations for the transconductance g_m of the MOS transistor is the following [8]:

(9) $$g_m = \sqrt{2\mu_n C_{ox} \frac{W}{L} I_D}$$

Taking into account that the dc drain current of M_1 and M_2 is equal to $I_{ss}/2$, for the G_m of the amplifier from Fig. 5 we obtain:

(10) $$G_m = \frac{g_m}{2} = \sqrt{2\mu_n C_{ox} \frac{W}{L} I_{D1}} = \sqrt{\mu_n C_{ox} \frac{W}{L} I_{ss}}$$

where W and L – the sizes of M_1 and M_2, μ_n – mobility of electrons and C_{ox} – gate-oxide capacitance.
The input impedance is determined by:

(11) $$Z_{in} = \frac{2}{sC_{gs}} = \frac{1}{sC_{in}}; \quad C_{in} = \frac{C_{gs}}{2}$$

as $C_{gs} = C_{gs1} = C_{gs2}$.

From Fig. 6 it can be seen that the output impedance consists of capacitance and resistance connected in parallel

(12) $$Z_o = R_o \| \frac{1}{sC_o}$$

as

(13) $$C_o = \frac{C_{db1}}{2} + \frac{C_{db3}}{2} + \frac{C_{dg3}}{2}$$

(14) $$R_o = 2\frac{r_{o1} r_{o3}}{r_{o1}+r_{o3}}$$

If r_{o1} and r_{o3} are replaced by the following equation

(15) $$r_o = \frac{1}{\lambda I_D}$$

Then the output resistance is

(16) $$R_o = \frac{4}{(\lambda_1+\lambda_3)I_{ss}}$$

where the λ is the slope of the output characteristic.

Key parameters of OTA related to the design of gyrator based G_m-C filters

Depending on the applications, designers choose between the importance of the following key parameters: control of G_m, output resistance R_o, linearity, DC stability.

- ***Control of G_m***

The easiest way to control G_m is by using the tail current I_{ss}, according to (10) However, in the formula we have a square root of this current and in order to obtain a large change of G_m, a large value of I_{ss} is required. This relationship depends on the linearization method of the I-V characteristic of the OTA.

The second option is to change the transistors W / L ratio. This can be achieved by placing several stages connected in parallel as shown in Fig.7 [9] [10].

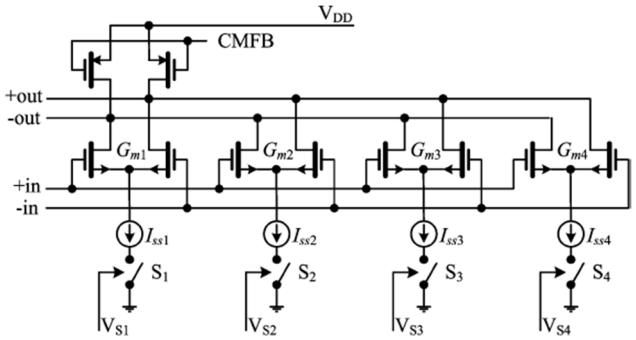

Fig. 7. Example of OTA, consisting four switching differential pairs connected in parallel [7].

They are switching on, when the current I_{ss} flows in them and they are switching off, when the current I_{ss} stops. These currents and the sizes of the pairs must be such that G_{m1}:G_{m2}:G_{m3}:G_{m4} = 1:2:4:8. Then the equivalent G_m is regulated evenly from G_{m1} to 15×G_{m1} with a step of G_{m1}. The active load is common for all pairs. Each pair can have a separate active load, which also needs to be switched on/off.

Another opportunity to control G_m is by parallel connecting of the transistors in the differential pair and switching the appropriate transistors [11]

- ***Output resistance***

In the design of gyrator based G_m-C filters the capacitors are connected in parallel to the OTA outputs. The capacitive component of the output impedance becomes part of this capacitor. The resistive part appears in parallel to this capacitor and can change some of the filter parameters – usually it decreases the pole's quality factor.

As mentioned before, the current I_{ss} in (10) is often used for tuning the transconducatance G_m for a single stage OTA. From this formula it can be seen that the dependence of G_m from I_{ss}, simultaneously influences the output resistance R_o. In order to avoid this double influence over R_o, R_o should have large value enough to keep the filter parameters unchanged.

The increase of R_o can be realized by the following methods: (i) by using cascode circuit in the OTA output stage [12]; (ii) by placing a negative resistance in parallel to the OTA output.

The differential cascode amplifier used for the increasing of the output resistance is shown in Fig. 8 [8], [13]. As it can be seen from the same figure, the number of the active elements is increased, which leads to an increased power consumption.

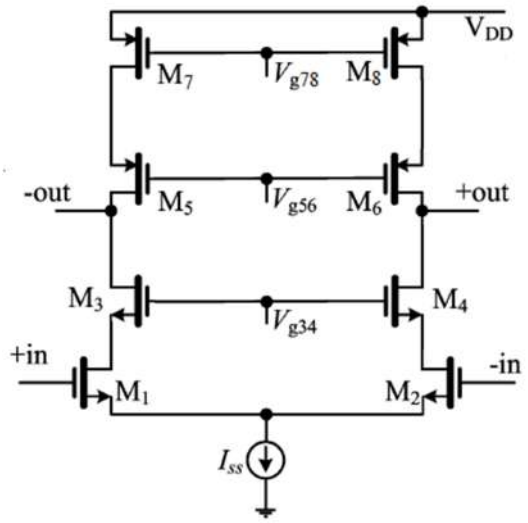

Fig. 8. Differential cascode amplifier.

The OTA with negative resistance connected in parallel to the output is shown in Fig.9. The negative resistance is formed by transistors M_5 and M_6. For stability reasons, this resistance needs to be less than the output resistance determined by transistors M_1 and M_4. In this circuit G_m is controlled by the current I_{ss} and the output resistance with I_{ss1} [8], [14].

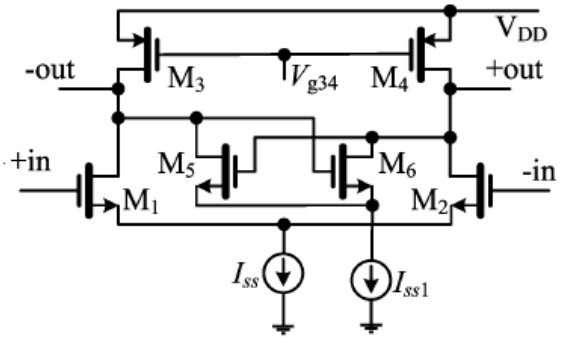

Fig. 9. Differential stage with added negative resistance parallel to the output.

• ***Linearity***

One of the main problems in transconductance amplifiers is the achieving of good linearity. This problem is caused by the nonlinear dependence of the drain current on the gate voltage of the transistors in the amplifier and the necessity for operation at low supply voltages. The nonlinear dependence leads to a nonlinear distortion of the output AC signal. It limits the maximum amplitude of the OTA output signal and its dynamic range. Many efforts have been invested in transconductor linearization methods and the progress is substantial: the first proposed OTAs had a maximum input voltage of 30 mV, while nowadays the achieved linear range is about 1 V at significantly lower supply voltages [2], [13].

There are many methods for linearization of the OTA I-V characteristic, but the most commonly used are the following two: placing degeneration resistors and cross-coupled differential pairs.

In the first method degeneration resistors are placed in the sources of the OTA's output stages where the signal is largest [8], [15]. In this way, a negative feedback is created.

The differential amplifier circuit with included degeneration resistors and its modification is shown in Fig. 10.

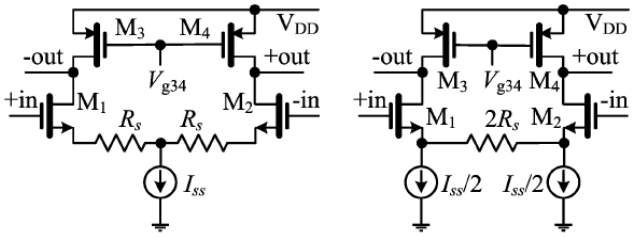

Fig. 10. (a) Differential amplifier with included degeneration resistors R_s (b) modification of the circuit aimed at avoiding the dc voltage on the resistors R_s.

The main advantage of this method is its simple structure. Usually, resistances are realized with MOS transistors operating in the linear region. They give better linearity of this circuit, but the equivalent transconductance G_m of the circuit is decreased [16]. It decreases according to the formula

$$G_{m,deg} = \frac{G_m}{1+2G_mR_S} \tag{17}$$

where $G_{m,deg}$ is the value of the transconductance with included resistances R_s. In Fig.10 (a) the dc voltage on the resistances R_s leads to the decrease of the maximal allowed output differential voltage needed for normal operation [17]. It could be compensated with increase of the supply voltage. This effect is avoided in the circuit from Fig. 10 (b), due to the absence of the current flow thought the resistor $2R_s$, when the input differential voltage is zero [18], [19].

The second method for linearization of the OTA I-V characteristic is shown in Fig. 11. The OTA core consists of two differential pairs, whose outputs are cross-coupled [16], [18], [19], [20], [21], [22]. This method is based on subtraction of the output currents of the pairs, because of the cross connection of the OTA outputs

$$I_o = I_{o,a} - I_{o,b} \tag{18}$$

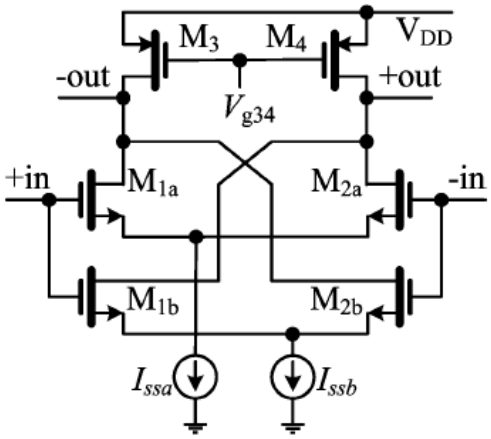

Fig. 11. OTA with cross-coupled differential pairs.

For fully differential amplifiers, the output current is an odd function of the input voltage:

$$I_o(V_{in}) = -I_o(-V_{in}) \tag{19}$$

This means, that it can be approximated by a polynomial having only odd degrees of V_{in}:

$$I_o = (G_{m,a} - G_{m,b})V_{in} + (A_{3,a} - A_{3,b})V_{in}^3 + +(A_{5,a} - A_{5,b})V_{in}^5 + \cdots \tag{20}$$

The parameters G_m, A_3, A_5 , etc. are function of the transistor sizes of the pairs and the currents flowing through them. The transistors in the differential pairs need to be matched. This condition, together with the value of the tail current, must be chosen in a way ensuring canceling the nonlinear component V_{in}^3. For these two conditions to be satisfied, a strict relationship between the parameters of the two pairs should be kept. The terms with higher degrees are not neglected; they have influence at significantly higher values of V_{in}.

Therefore, this method is dependent on the pvt (process, bias voltage and temperature) changes. Similarly, to the previous method, in this method a decrease of the transconductance G_m is observed.

There are other methods for linearization in addition to the above two [13]. Such an additional

method is the one based on a differential pair, which operates in triode region and in that way, it is biasing the source dc voltage [23], [24]. Another method is using adaptive biasing of the tail current [25]. In this method, the dc voltage must be stabilized. There is also a method with bulk driven is proposed in [26], where additional elements such as amplifiers are placed in each arm of the pair to form a feedback.

Some solutions use two different linearization techniques in the same OTA. For example, combination of the method with the source degeneration resistors and the method with the cross-coupled differential pair [18], [19].

- ***DC stability***

The differential amplifiers with active load have problems with the stability of the dc output voltage. This voltage significantly changes at small variations of the tail current I_{ss}, the voltage of the active load V_{g34} (Fig. 5), the temperature, the supply voltage etc [16].

The reason for the instability: the load line determining the drain-to-source voltage of the main differential pair in Fig. 5 is part of the output characteristics of the transistors in the dynamic load. The operating point of transistors M_1 and M_2 is determined by the intersection points of their output characteristics and the load line obtained from the corresponding output characteristics of M_3 and M_4. All transistors are in active regime and the intersection happens in the region, where the slope of the lines is very small. In that case, a small change in the parameter causes a significant displacement of this point.

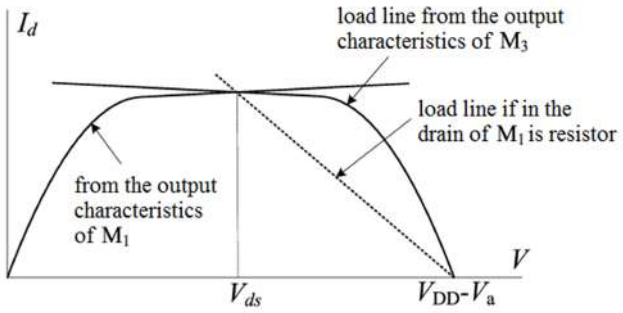

Fig. 12. The reason for the instability in the dc output voltage for the circuit in Fig. 5.

For comparison purposes, in the Fig. 12 the load line is shown if a resistor is placed instead of M_3. It can be seen that the angle of intersection with the output characteristic of M_1 is larger and the voltage V_{ds} is more stable.

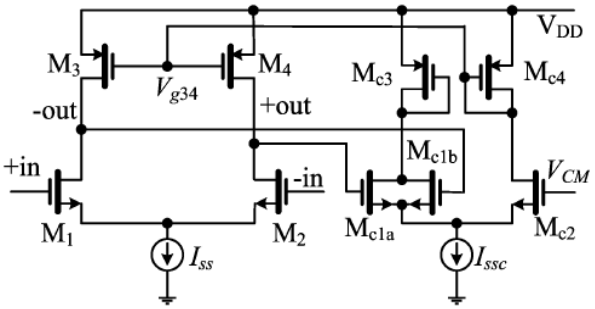

Fig. 13. Differential OTA with included CMFB.

The stabilization of the output dc voltage is done by adding common-mode feedback (CMFB). In Fig. 13 two differential OTA with different implementation of the CMFB are shown [8], [14]. The dc voltages of the two outputs (–out and + output) are averaged and the averaged voltage is fed to another differential amplifier [12].

The disadvantage of the circuit in Fig. 13 is that the additional gate-source capacitance of transistors M_{c1a} and M_{c1b} is inserted.

Comparison between single stage and multiple stage OTA with respect to frequency dependence

The frequency range in which OTAs can operate is finite. The limitation can from the frequency dependence of G_m and/or additional parasitic capacitances.

Single stage OTA has higher upper limit for the frequency due to appearance of transient capacitance C_t. However, large G_m values require larger transistors sizes (W/L) and larger dc currents.

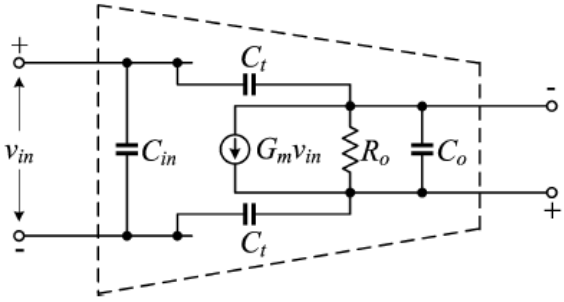

Fig.14. Equivalent circuit of a single stage OTA.

For a single stage OTA, the frequency dependence of G_m given by

$$G_m = G_{m0}(1 - s\tau) \quad (21)$$

where $\tau = C_t/2G_{m0}$.

Multiple stage OTA can achieve higher G_m easier. However, the interface between stages creates pole, which limit the frequency of operation.

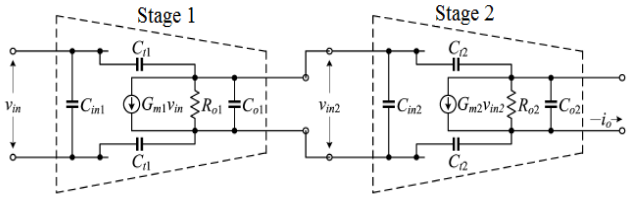

Fig.15. Block circuit of a two stage OTA.

For multiple stage OTA (Fig. 15), the frequency dependence of G_m is given by

$$G_m = \frac{G_{m01}G_{m02}R_{01}}{1+\frac{s}{\omega_b}} \quad (22)$$

The analysis of the frequency dependence of G_m reveals that for single stage OTAs the frequency dependence is approximated by a single positive zero, while for multiple stage OTAs – it is approximated by a single negative pole.

This means that G_m in the single stage OTA increases at very high frequencies, while in the multiple stage OTA it decreases. The frequency at which G_m starts to change is lower in multiple stage OTAs than the frequency in single stage OTAs; hence, multiple stage OTAs are more suitable for operation at lower frequencies, while single stage for higher frequencies.

However, the multiple stage OTAs give larger values for G_m; this is required in filters intended for operation at very high frequencies.

Applications

Hertz and sub-Hertz frequency range is appropriate for digital filters. In these cases a very small processing speed is needed and any processor can be used. However, digital filters require several satelite blocks: ADC and DAC, clock generators. All of them are increasing the circuit power consumption. For this reason, analog filters are preferably used in applications where power consumption is cruical: bio-medical devices, esspecialy implantabile devices, remote long working sensors, etc.

The values of the components determining the pole frequency are adjustable enabling frequencies from 1 Hz to hundreds of MHz. Since the $\omega_p = G_m/C$, for very low frequencies tens of pF and nS or pF and hundred of pS are required [27].

The increase of the frequency requires higher values of G_m, which leads to the increase of the bias current.

Table 1

Gyrator based G_m-C filters for low frequency applications

	[17]	[18]	[19]	[21]	[28]
Year	2016	2009	2000	2011	2016
Filter Type	BPF	LPF	LPF	BPF	BPF
Technology CMOS [µm]	0.18	0.18	0.8	0.35	0.18
Order	4th	5th	6th	7th	4th
Supply voltage [V]	1	1	1.5	1	1
Bandwidth [Hz]	212	-	-	1	-
Center frequency [Hz]	0.3k-2.4k	240	2.4	1-64	80-6.18k
Power Consumption [W]	61n	453n	10µ	60p	462p
Dynamic Range [dB]	52	50	60	43	57.6
THD [dB]	-50.23	-48.6	-50	-	-

Table 2

Gyrator based G_m-C filters for high frequency applications

	[12]	[16]	[22]	[29]
Technology	0.25µm	0.13µm	0.18µm	28nm
Filter Type	LPF	LPF	LPF	LPF
Order	4th	2nd	3rd	3rd
Supply voltage [V]	3.3	1.2	1.8	0.7-1
Center frequency [MHz]	65-350	200	50-300	454-459
Power Consumption [mW]	70	20.8	205.2	4-5.6
Dynamic Range [dB]	54	-	73.5	-
In-band gain [dB]	-	0	0	-0.7 to -0.3

Conclusion

G_m-C filters with gyrators are widely popular in modern integrated circuit design for simulating the presence of inductors in LC circuits. In this paper we reviewed the types, architecture, and properties of gyrator based G_m-C filters. The most significant parameters of OTA related to G_m-C filters are

considered - control of G_m, output resistance, linearity, and DC stability. We summarized various techniques for optimizing OTA parameters.

A comparison between single stage and multiple stage OTAs was performed with respect to frequency dependence of G_m. The multiple applications for very wide frequency range starting from few Hz (biomdeical devices) up to several hundred of MHz (wireless communications) were outlined.

Acknowledgement

This work was supported by project BG05M2OP001-1.001-0008-C01/28.02.2018 "Creation and Development of Centres of Excellence"- "National center of mechatronics and clean technologies".

REFERENCES

[1] T. Deliyannis, Y. Sun and J. Fidler, Continuous-Time Active Filter Design, CRC Press, 1999.

[2] T.-Y. Lo and C.-C. Hung, 1V CMOS Gm-C Filters: Design and Applications, Springer, 2009.

[3] H. G. Dimopoulos, Analog Electronic Filters: Theory, Design and Synthesis, Springer, 2012.

[4] Y. Sun, Ed., Design of High Frequency Analog Integrated Filters, The Institutions of Electrical Engineers, 2002.

[5] P. V. A. Mohan, VLSI Analog Filters: Active RC, OTA-C and SC, Springer, 2013.

[6] R. Schaumann, H. Xiao and M. V. Valkenburg, Design of Analog Filters, 2nd ed., Oxford university Press, 2009.

[7] I. Uzunov, Course of Analog Filters, 2018.

[8] B. Razavi, Design of Analog CMOS Integrated Circuits, McGraww-Hill, 2016.

[9] A. S. Korotkov, D. V. Morozov, A. A. Tutyshkin and H. Hauer, "Channel filters for microelectronic receivers of wireless systems," in 2005 IEEE 7th CAS Symposium on Emerging Technologies: Circuits and Systems for 4G Mobile Wireless Communications, 2005.

[10] I. Uzunov, A. Tanev and M. Hristov, "Design and Investigation of Tunable Gyrator Resonance Circuit Implemented on AMS 0.35µm Process," WSEAS Transactions on Circuits and Systems, vol. 16, pp. 45-54, 2017.

[11] P. Crombez, J. Craninckx, P. Wambacq and M. Steyaert, "A 100-kHz to 20-MHz Reconfigurable Power-Linearity Optimized Gm–C Biquad in 0.13-µm CMOS," IEEE Transactions on Circuits and Systems II: Express Briefs, vol. 55, no. 3, pp. 224-228, 2008.

[12] S. Pavan and Y. Tsividis, High Frequency Continuous Time Filters in Digital CMOS Processes, Springer, 2000.

[13] E. Sanchez-Sinencio and J. Silva-Martinez, "CMOS transconductance amplifiers, architectures and active filters: a tutorial," IEE Proceedings - Circuits, Devices and Systems, vol. 147, no. 1, pp. 3-12, 2000.

[14] T. C. Carusone, D. Johns and K. Martin, Analog Integrated Circuit Design, 2nd ed., Wiley, 2012.

[15] A. Lewinski and J. Silva-Martinez, "A High-Frequency Transconductor Using a Robust Nonlinearity Cancellation," IEEE Transactions on Circuits and Systems II: Express Briefs, vol. 53, no. 9, pp. 896 - 900, 2006.

[16] M. Mobarak, M. Onabajo, J. Silva-Martinez and E. Sanchez-Sinencio, "Attenuation-Predistortion Linearization of CMOS OTAs With Digital Correction of Process Variations in OTA-C Filter Applications," IEEE Journal of Solid-State Circuits, vol. 45, no. 2, pp. 351-367, 2010.

[17] H.-C. Chu, Y.-H. Huang and C.-C. Hung, "Low-power CMOS bandpass filter for application of cochlear prosthesis," in 2016 IEEE 59th International Midwest Symposium on Circuits and Systems (MWSCAS), 2016.

[18] S.-Y. Lee and C.-J. Cheng, "Systematic Design and Modeling of a OTA-C Filter for Portable ECG Detection," IEEE Transactions on Biomedical Circuits and Systems, vol. 3, no. 1, pp. 53-64, 2009.

[19] S. Solis-Bustos, J. Silva-Martinez, F. Maloberti and E. Sanchez-Sinencio, "A 60-dB dynamic-range CMOS sixth-order 2.4-Hz low-pass filter for medical applications," IEEE Transactions on Circuits and Systems II: Analog and Digital Signal Processing, vol. 47, no. 12, pp. 1391 - 1398, 2000.

[20] A. Lewinski and J. Silva-Martinez, "OTA linearity enhancement technique for high frequency applications with IM3 below -65 dB," IEEE Transactions on Circuits and Systems II: Express Briefs, vol. 51, no. 10, pp. 542 - 548, 2004.

[21] P. Corbishley and E. Rodriguez-Villegas, "A Nanopower Bandpass Filter for Detection of an Acoustic Signal in a Wearable Breathing Detector," IEEE Transactions on Biomedical Circuits and Systems, vol. 1, no. 3, pp. 163 - 171, 2007.

[22] K. Kwon, "A 50- to 300-MHz CMOS Gm-C Tracking Filter Based on Parallel Operation of Saturation and Triode Transconductors for Digital TV Tuner ICs," IEEE Transactions on Circuits and Systems II: Express Briefs, vol. 62, no. 6, pp. 522-526, 2015.

[23] T.-Y. Lo, C.-C. Hung and M. Ismail, "A Wide Tuning Range Gm–C Filter for Multi-Mode CMOS Direct-Conversion Wireless Receivers," IEEE Journal of Solid-State Circuits, vol. 44, no. 9, pp. 2515-2524, 2009.

[24] H. Tanaka, K. Tanno, H. Tamura and K. Murao, "Design of CMOS OTA for Low-Voltage and Low-

Power Application," IEICE Trans. Fundamentals of Electronics, Communications and Computer Sciences, Vols. E-91A, no. 11, pp. 3385-3388, Nov. 2008.

[25] K. R. Ajayan and N. Bhat, "Linear transconductor with flipped voltage follower in 130 nm CMOS," Analog Integrated Circuits and Signal Processing, vol. 63, no. 2, p. 321–327, 2010.

[26] L. Zhang, X. Zhang and E. El-Masry, "A highly linear bulk-driven CMOS OTA for continuous-time filters," Analog Integrated Circuits and Signal Processing, vol. 54, no. 3, pp. 229-236, 2008.

[27] A. Veeravalli, E. Sanchez-Sinencio and J. Silva-Martinez, "Transconductance amplifier structures with small transconductances: a comparative design approach," IEEE Journal of Solid-State Circuits, vol. 37, no. 6, pp. 770-775, 2002.

[28] Y. Sundarasaradula and A. Thanachayanont, "A 1-V, 6-nW programmable 4th-order bandpass filter for biomedical applications," Analog Integrated Circuits and Signal Processing, vol. 89, no. 1, pp. 89-98, 2016.

[29] J. Lechevallier, R. Struiksma, H. Sherry, A. Cathelin, E. Klumperink and B. Nauta, "5.5 A forward-body-bias tuned 450MHz Gm-C 3rd-order low-pass filter in 28nm UTBB FD-SOI with >1dBVp IIP3 over a 0.7-to-1V supply," in 2015 IEEE International Solid-State Circuits Conference - (ISSCC) Digest of Technical Papers, 2015.

M.Sc. Eng. Atanas Tanev *obtained his BSc degree in 2009 with the highest honor as a student with best achievements. The MSc degree in Electronic Engineering was completed in 2011 with very high GPA result. Both BSc and MSc are obtained from the Technical University of Sofia, Branch Plovdiv. Between 2012 and 2016 A. Tanev is a PhD student in Department of Microelectronics, Faculty of Electronic Engineering and Technologies, Technical University of Sofia. In 2013 and in 2014 he was Guest Researcher in Philips Research, Eindhoven, the Netherlands. His research interests include modern innovative analog integrated circuits design, analog signal processing and programmable analog circuits.*

e-mail: atanev@ecad.tu-sofia.bg

Reveived on: 31.05.2018

In-flight sensor system for collecting flight information and providing flight safety of unmanned aerial system

Krume Andreev, Rumen Arnaudov, Ivo Dochev

In the last decade there has been a rapid development of unmanned aerial aviation and various solutions are sought for gathering information from difficult access points or in cases where there is a risk to operators and technology. This article looks at a solution for the implementation of an in-flight sensor system for collecting in-flight data of the unmanned aerial system ensuring flight safety. The characteristics of these systems are studied and an architectural realization of a flight and safety control platform for unmanned aircraft is proposed.

Keywords – sensor system, flight safety, measurement systems.

Сензорна система за събиране на информация по време на полет на безпилотен летателен апарат за обезпечаване на безопасност на полета (Круме Андреев, Румен Арнаудов, Иво Дочев). *През последното десетилетие се наблюдава бурно развитие на безпилотната летателна авиация и се търсят различни решения за събиране на информация от обекти с труден достъп или в случаи, при които съществува риск за операторите и техниката. Настоящата статия разглежда едно решение за апаратна реализация на сензорна система за събиране на информация по време на полет на безпилотен летателен апарат за обезпечаване на безопасност на полета. Проучени са характерните на тези системи и е предложена архитектурна реализация на платформа за контрол на полета и на безопасността на безпилотен летателен апарат.*

Introduction

In the last decade there has been a rapid development of unmanned aerial aviation and various solutions are sought for gathering information from difficult access points or in cases where there is a risk to operators and technology. Companies producing this type of aerial vehicles are seeking to refine unmanned aerial systems which are already in service and develop new ones. One option to solve this problem is the use of unmanned aerial systems (UAS), such as gliders and copters (Figure 1). They are characterized by high mobility, unlimited in time and space access to information, and the need to monitor their condition. Numerous tasks can now be identified, the investigation and solution of which presupposes the use of UAS, each having an operational and / or permanent nature. Unmanned aerial systems may be used in [1]:

• Events of accidents and disasters, the detection of victims and the monitoring of the region in distress;

• Agriculture for sighting crops, recording the condition of agricultural crops after caused damage of various kinds, searching for lost animals, monitoring of the farm, etc;

• Surveillance systems for monitoring of the large territories, etc;

• Ecology for monitoring the state of flora and fauna, recording of damage caused by illegal felling of forests, etc;

• Monitoring the status of areas affected by natural disasters and assessing damages from: spills and floods, dams overflow, forest fires, earthquakes, industrial accidents, destroyed bridges / roads, etc;

• Monitoring of: protective equipment (dykes, enclosures); the process of restoration of burnt areas; monitoring of recultivated areas; monitoring of dam walls, etc;

• Capture of the current state of the plots of the agricultural cadastre (updating of the orthophoto map of the agricultural land), etc;

• In the field of energy for: recording of damage and icing on the electricity transmission network, recording of damage to the oil / gas network,

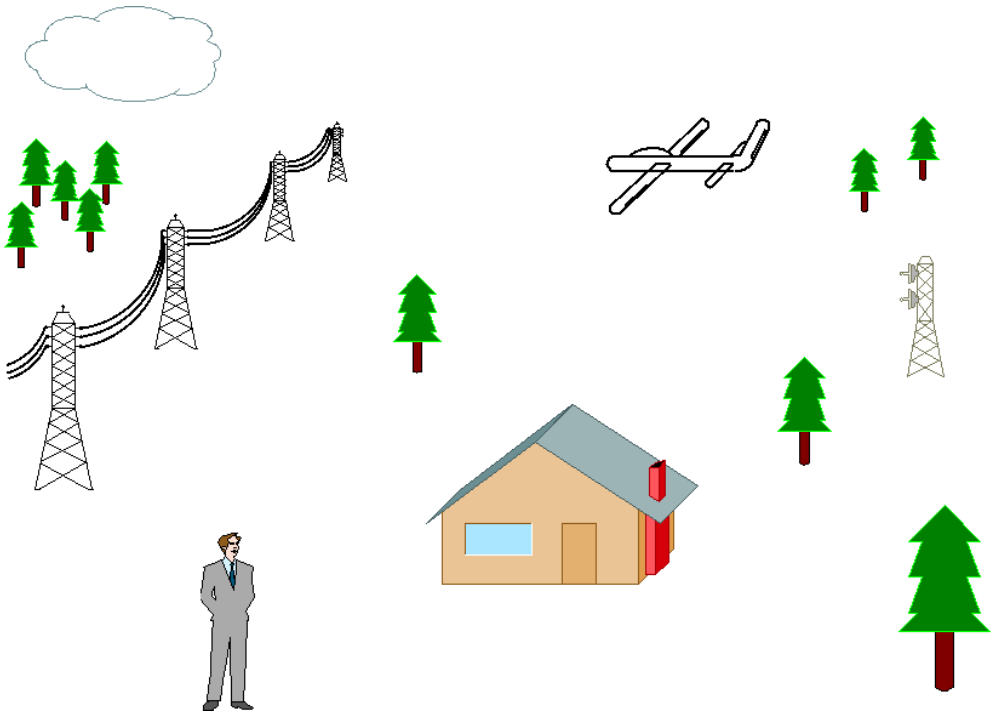

Fig.1. Use of unmanned aerial system to collect information from difficult access points or in cases where there is a risk to operators and technology.

monitoring of the routes of the electricity transmission and the oil / gas transmission networks, etc;

Unmanned aerial systems can only be used if they can effectively complete their mission and respond to problematic and precarious environmental conditions [2]. One important condition that must always be observed is that it is imperative to maintain safety with regard to other aircraft, people and objects on the ground.

Highly relevant for this purpose is the development of sensors systems for gathering information during the flight of the unmanned aerial system to ensure flight safety.

The unmanned flight system of the practice is a union of three basic subsystems [3], the structure of which is determined by the objectives and tasks set.

The first subsystem of UAS is the aircraft, which, depending on the constructive solution, can be:

- "Fixed wing" aircraft;
- "Rotating wing" aircraft;
- Aircraft lighter than air (airship);

In addition to the above mentioned variants, various attempts are made to construct “wing flying” aircraft resembling the movement of bird wings. The main types of power models are operated by an electric motor, an internal combustion engine, a fuel cell or a reactive engine [4].

The second subsystem of the UAS is the navigation system that allows a single (or assisted) controlled flight to be performed on a predetermined route or route that is constructed at the time of flight. The navigation subsystem allows a controlled flight to be monitored, captured, measured, etc., activities enabling retrieval of scientific information on the presence, position or status of the research object or phenomenon. The navigation subsystem includes: autopilot and positioning device (GPS) [5].

The third subsystem of UAS is made up of different instruments and tools for capturing, recording and measuring, parameters for assessing spatial dimensions, position or state of various objects and phenomena. Depending on the objectives, this subsystem may be deployed only on-board the aircraft or be composed of two segments: an on-board segment and a ground segment. In the latter case, the on-board segment is complemented by a transmitting element, which allows the real-time telemetry information to be transmitted to the receiving segment from the ground segment. In the presence of a transmitting element, the function of the navigation system can also be enriched by providing feedback allowing visualization of the flight parameters and the operation of the aircraft [6].

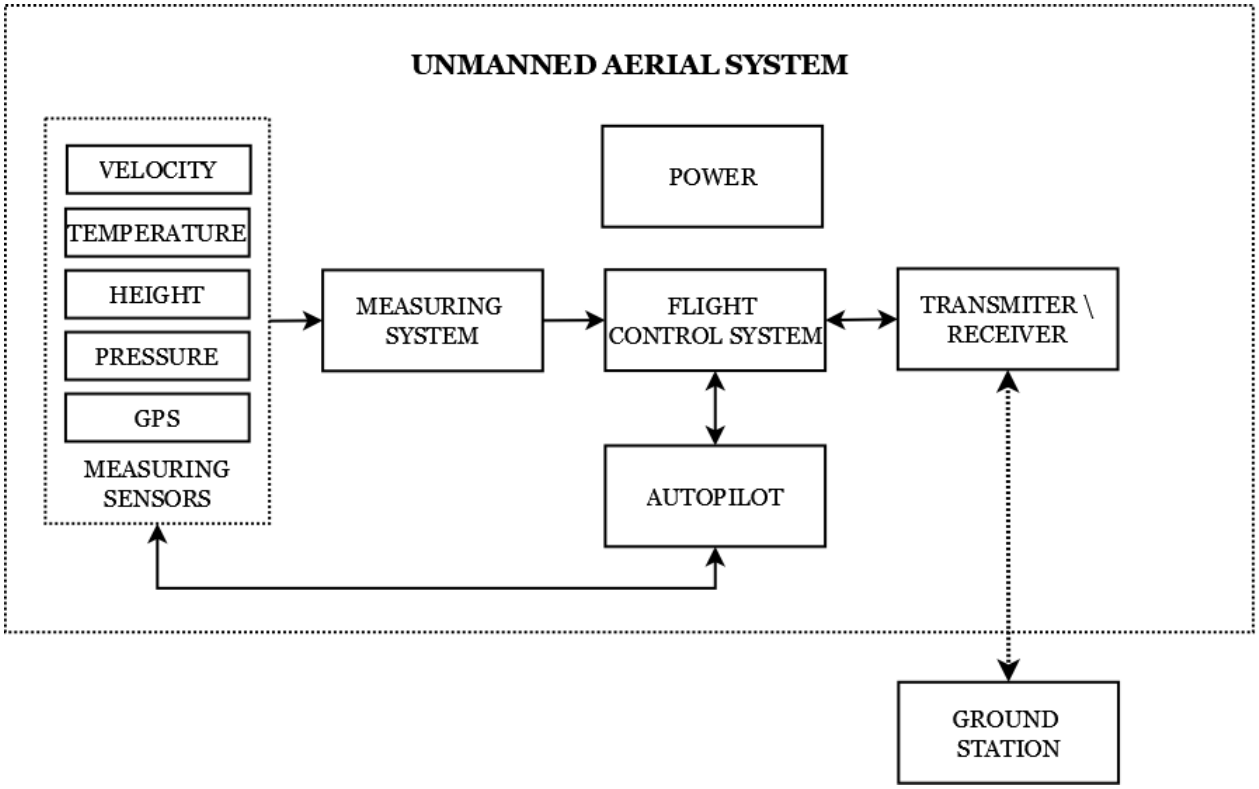

Fig.2. Architecture of the In-flight sensor system for collecting flight information providing flight safety.

Such a system should be able to perform the following tasks [7]:

- To monitor multiple sensory and software signals in dynamic mode;
- On the basis of the collected measurement information from on-board systems, to be possible to perform the control and and report diagnosis of defects;
- When getting outside of the the operator range, the system automatically switches to autopilot mode.
- The electronic systems used in the UAS must comply with the normative requirements for electro-magnetic compatibility.

Construction of a platform for unmanned aerial systems

A gliders or copters can be used to build a pilotless aircraft system. Planners have a relatively high load capacity and flight duration but do not have much maneuverability. Copters are characterized by great maneuverability, but they do not have high payload and flight duration.

The basic principles for building unmanned aircraft systems are:

- Creating a modular, light platform with low power consumption;
- Real-time monitoring of sensors and software signals;
- Analysis of received information and in-flight preprocessing.

Another important feature in the choice of the unmanned aircraft and the in-flight sensor system for collecting information to provide flight safety is the ability of the established platform to comply with the country's flight rules. At this stage in Bulgaria, these rules are being developed. Flight rules are defined by national and international institutions, for example, for the United States, it is the Federal Aviation Administration [8]. Some of the parameters in this policy are: the minimum height that aircraft after take-off, maximum flight speed, landing time, etc. have to reach;

The architecture of the in-flight sensor system for collecting flight information providing flight safety is presented in fig. 2. It contains: measuring sensors, measuring system, flight control system, transceiver, autopilot and remote control terminal. With the help of the measuring sensors, the flight parameters and the condition of the aircraft, its coordinates and the environmental parameters are monitored. For this purpose the following sensors are used:

- GPS receiver. It helps determine the

location of the aircraft.

- Temperature sensor. In this case, the presence of hot air currents is monitored.
- Air velocity sensor. This parameter is important because it can further control the speed of UAS.
- Barometric pressure sensor. This height and speed can be monitored via the Z axis.
- Laser altimeter for height measurement.
- Ultrasonic radar to prevent the unmanned airplane from colliding with other or other flying objects.
- Accelerator accelerometer for acceleration of unmanned aircraft in case of a sudden loss of lifting force or impact of a UAS on another object.
- Magnetometer that measures the Earth's magnetic field as a inertial navigation signal;
- Alarm system. With this system, if a UAS falls, the sound is signaled for the uncontrolled fall of the UAS.

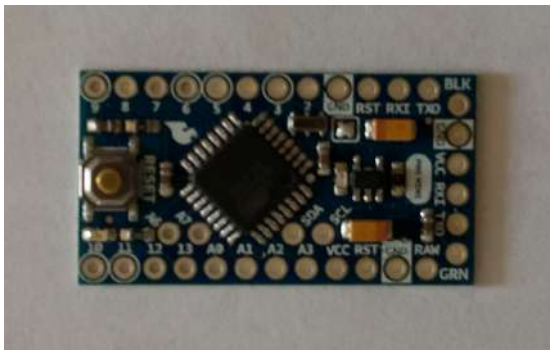

Fig.3. Development platform Arduino Uno.

The microcontroller, which is used as a measuring system, processes the received information from the sensors, forms commands to the flight control system and telemetry to the ground station operator. The measured parameters are duplicated on one of the sensors in order to monitor the accuracy of their measurements using reference monitors. The measuring system was built using the Arduino mini development platform (Figure 3) [9]. In addition to semi-autonomous and autonomous flight mode, the autopilot aims to take control of the control when the planer comes out of the range of manual control. If possible, he may complete the mission and return the unmanned instrument to the take-off point or other predefined coordinates. With the transceiver, commands are given to manually control the flight from the remote control terminal, and information is sent to the flight operator.

Collection and processing of results data

Table 1 presents the collected data from the comparative tests of 4 quad-copters and 1 glider. The maximum flight times achieved to a large extent depends on:

- The unmanned aerial system carrying capacity, including its weight;
- Battery capacity;
- Additional equipment mounted;
- Force and direction of wind.

Table 1

Comparative test data

Unmanned aerial system:	Weight of the UAS:	Weight of the battery:	Total weight:	Battery capacity:	Max. flight time:
Quadcopter LS-122	**111 g**	**18 g**	**129 g**	**3,7 V / 600 mAh**	**8 min**
Quadcopter Yuxiang 668-A3	**100 g**	**10 g**	**110 g**	**3,7 V / 380 mAh**	**6 min**
Quadcopter RTF-2.4 GHz	**114 g**	**24 g**	**138 g**	**7,4 V / 400 mAh**	**12 min**
Quadcopter MJX BUGS 3	**371 g**	**114 g**	**485 g**	**7.4V / 1800mAh**	**15 min**
Planer F-1400 Upstream – PRE-Flight checklist	**520 g**	**80 g**	**600 g**	**11.1 V / 1300mAh**	**35 min**

Conclusion

This article examines an option for a solution of an in-flight sensor system for collecting flight information and providing flight safety. The features that these systems must meet and the architectural realization of a flight control platform on a pilotless airplane system are being explored. The implementation of the proposed platform will be applied in a wide range of areas such as: accidents and disasters, agriculture, ecology and security systems, etc.

Acknowledgement

Research project of the assistance to the PhD students (Session 2018 Second Stage) contract number 172ПД0005-07.

REFERENCES

[1] Musliner, D., J. Hendler, A. K. Agrawala, E. Durfee, J.K. Strosnider, and C.J. Paul. The challenges of real-time AI. IEEE Computer, 1995, pp. 58–66.

[2] Schumann, J., O.J. Mengshoel, and T. Mbaya. Integrated software and sensor health management for small spacecraft. In Proc. of the 2011 IEEE fourth international conference on space mission challenges for information technology, 2011, pp. 77–84.

[3] Poll, S., A. Patterson-Hine, J. Camisa, D. Garcia, D. Hall, C. Lee, and X.C. Koutsoukos. Advanced diagnostics and prognostics testbed. In Proc. of the 18-th international workshop on principles of diagnosis, dx-07, 2007, pp. 178–185.

[4] Zhao, Y., and K.Y. Rozier. Formal specification and verification of a coordination protocol for an automated air traffic control system. In Proceedings of the 12th international workshop on automated verification of critical systems (AVoCS 2012), Vol. 53, 2012, pp. 65-125.

[5] Schumann, J., O.J. Mengshoel, and T. Mbaya. Integrated software and sensor health management for small spacecraft. In Proc. of the IEEE fourth international conference on space mission challenges for information technology, 2011, pp. 77–84.

[6] Poll, S., A. Patterson-Hine, J. Camisa, D. Garcia, D. Hall, C. Lee, and X.C. Koutsoukos. Advanced diagnostics and prognostics tested. In Proc. of the 18th international workshop on principles of diagnosis (dx-07), Nashville, TN, 2007, pp. 178–185.

[7] Schumann, J., K.Y. Rozier, T. Reinbacher, O.J. Mengshoel, T. Mbaya, and C. Ippolito. Towards Real-time, On-board, Hardware-supported Sensor and Software Health Management for Unmanned Aerial Systems. 2013, pp.1-21.

[8] Federal Aviation Administration. Federal Aviation. Regulation §91, 2013.

[9] Arduino Foundation, (https://www.arduino.cc)

Eng. Krume B. Andreev, PhD student *is with the Faculty of Telecommunications at Technical University of Sofia, 8 Kl. Ohridski Blvd, Sofia 1000, Bulgaria.*

tel..:02 965 33 26 e-mail: Andreev.k@abv.bg

Prof. Dr. Rumen I. Arnaudov *is with the Faculty of Telecommunications at Technical University of Sofia, 8 Kl. Ohridski Blvd, Sofia 1000, Bulgaria.*

tel..:02 965 33 26 e-mail:ra@tu-sofia.bg

Assoc. Prof. Dr. Ivo N. Dochev *is with the Faculty of Telecommunications at Technical University of Sofia, 8 Kl. Ohridski Blvd, Sofia 1000, Bulgaria..*

tel. 02 965 21 46 e-mail: idochev@tu-sofia.bg

Received on: 28.05.2018

A remote controlled system implementation for object video monitoring

Ivo Dochev, Liljana Docheva, Maria Pavlova

In the current article a solution of the problem with information taking from difficult to reach and dangerous earth places is described. The robots will be very useful in this case. In the article hardware part researching and designing of such a system is done. The main modules are: a quad-copter and a control system. A modern technology allowed to survey the remotely objects is presented. The system can record information and after that transmit the data to the remotely work station. The problems, which appears in the research work and the solution for their solving is discussed. The possibilities for information transmission are considered. The proposed solution can be used in disasters, ecology projects, sports events, energy sectors and etc.

Keywords – control system, remote control, image recognition.

Възможност за реализация на дистанционно управлявана система за видеонаблюдение (Иво Н. Дочев, Лиляна Е. Дочева, Мария Ц. Павлова) *В настоящата статия е разгледана възможност за получаване на информация за обекти, разположени на трудно достъпни или опасни за хората части от земната повърхност. В този случай е полезно използването на роботи. В статията е разгледано проектирането и реализацията на дистанционно управлявана система за видеонаблюдение. Тя се състои от квадракоптер и система за управление. Информацията за наблюдаваните обекти може да се запише и да се предаде към отдалечена работна станция, където данните могат да се обобщят и обработят. Изложени са проблемите, които биха затруднили реализацията и експлоатацията на дистанционно управляваната система за видеонаблюдение. Обсъдени са възможностите за предаване на информацията към оператора. Тази система може да намери приложение в екологични проекти за опазване на околната среда, спортни мероприятия, енергетика и др.*

Introduction

The automated systems are widely used in our homes, industry, farming, environmental protection or water exploitation. It is difficult to control and manage automated systems in these cases and these operations usually are carried out remotely [1]. This in turn leads to the impossibility to be noticed changes in the working conditions end the working environment. Equipping such systems with video control and the appropriate sensors increases their capabilities by making them flexible and easy to manage.

The installation of a video observation system and sensors on various mobile objects with the possibility of remote control, allows reaching and monitoring of difficult to access and dangerous objects. This in turn creates the conditions for acquiring new scientific knowledge and for solving important issues in education, farming and ecology.

The remote-controlled system equipped with video observation system and appropriate sensors is able to solve problems like the insects control, disaster reaction, and hard meteorological conditions acquiring. It could help for prevention and improving the reaction if some of these events are happens again.

Many different factors and climatic conditions have influence of the environment. Using a video monitoring remote-controlled system equipped with appropriate sensors makes it possible to reach and observe the unapproachable places, including protect natural objects, where the human access is denied. This gives the possibility to acquire information about the changes that occurs in the environment and allows evaluating their impact in real time. This would provide useful information for their protection.

The collected data will create a data base which contains important information for making of new scientific knowledge in the field of education. The

students could use the data and that will give them the opportunity to face things they would never be able to without the remote observing system. Moreover they could take a part in the remote controlling and monitoring some of the processes. The data base could be used from the students and that will give them the opportunity to solve a problems and make decisions in situations that they couldn't reach without the remote observing system.

System architecture

The remote controlled video observation system could be used for electricity network breakdowns tracking, for water supply networks sources monitoring, for forest fires monitoring and a number of other areas where the object reaching of it is quite expensive. Fig. 1 presents one of the possibilities for practical application of a system for remote controlling of difficult accessible objects.

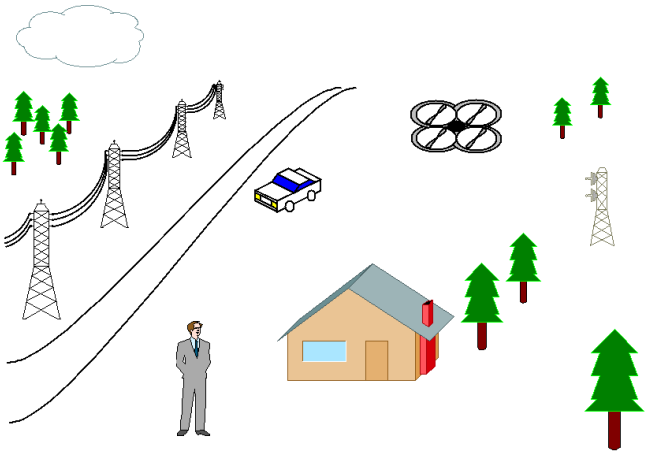

Fig.1. A remote controlled system application.

According to the investment and selected equipment the opportunities in such a system can significantly increase which in turn leads to expansion of its application. The quad-copter should be chosen according the possibilities to fly under sufficient big area for monitoring. With the quad-copter capacity increasing its ability to be in the air longer and to collect video information that can subsequently be processed and available for use increases too. The use of additional sensors may make it possible to collect as much information as possible with one flight of the quad-copter. The coordinate transmission of the monitoring place is an additional advantage of the control system. A real-time data and video information transfer increases the system capabilities. The video information storage, in turn, prevents the loss of information because of interruption in transmitting channel.

Figure 2 presents the remote controlled system architecture. The system contains following modules: a camera for objects capturing, a development platform; an external memory for information storing, a GPS module and sensors for coordinates transmission location to the development platform, a power supply, a transceiver that provides the connection to a remote terminal, a power supply for the control module; flight control module, a transceiver for the remote control.

The camera has the option to work in two main software modes: image capturing and video recording. The generated data in the second mode are too large and it takes a lot of memory to store this information. This problem can be solved by compressing video information.

The second part of fig. 2 includes a power supply-2, a receiver-transmiter-2- and a remote control module. The quad-copter is managed through remote control and receiver-transmiter-2, which gives information to flying control module.

The data from the microcontroller are transmitted by a wireless network to a workstation and vice versa. The development model for the application works with LINUX operation system.

This architecture gives the opportunity for different development applications.

On figure 3 a quad-copter is shown as an option to mount the hardware platform. From the propeller size and the quad-copter battery capacity depends :

- The perimeter that can be monitored by the remote control system;
- The weight that can be lift, which in turn determines the quantity and type of sensors and equipment that could be mounted on it.
- The quad-copter flight stability which affects the quality of video capture.

A lot of the commercially available quad-copters have built-in cameras and factory software does not support additional image processing. This requires the use of a dedicated development system that allows image recognition. The camera that is used of the development system is 8 MP "NoIR Camera V2" (fig. 4). One has the ability to capture images in the infrared spectrum [5]. The image resolution can be selected between 1080p 30fps, 720p 60fps and 640x480p 90fps. The camera weight is about 3 gr. The camera's size and weight are very important for mobile applications [2].

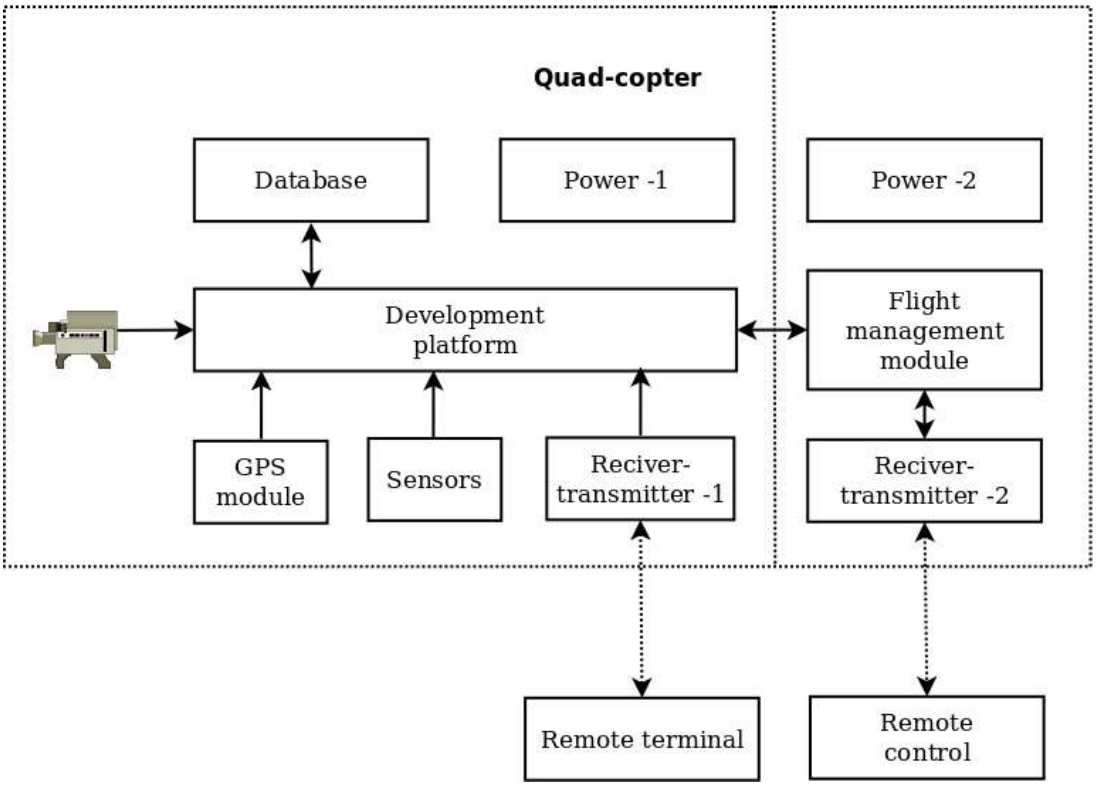

Fig.2. Architecture of the remote controlled system.

Fig.3. A Quad-copter.

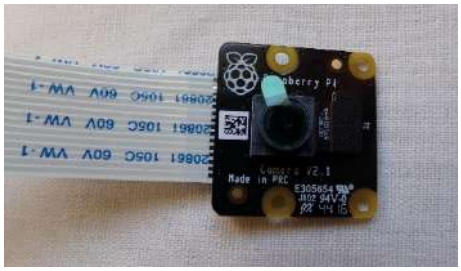

Fig.4. Video camera.

The received information from the camera is processed by development platform (fig. 5). One is attached to the quad-copter. A remote terminal controls the development platform by means of transmitter-receiver. The location of the system is transmitted to the development platform via the GPS module. It has the following features: 66 channel, small size, lightweight and compact, making it applicable to unmanned aerial vehicles.

Fig.5. Attached development platform to quad-copter.

The information from the camera is recorded in a memory. This creates a data base that can be used for data processing. Furthermore saving video information in development platform can prevent

information loss in the case of losing the connection through the channel.

A basic requirement for all elements attached to a quad-copter is a small weight, because the weight increasing affects the perimeter that can be monitored by the remote controlled system. This, in turn, guarantees a maximum mobility.

The microcontroller of the development platform is appropriate, because it is light and compact (fig. 6) [3]. The microcontroller has 4 core processor; 1 GB RAM; Wi-Fi module, low-energy consumption Bluetooth; 40 pin extended GPIO; 4xUSB 2 ports; HDMI; CSI camera port; DSI port for display; CD port that is used for loading of operation system and saving of information; USB power supply.

Fig. 6. The development platform "Raspberry Pi 3".

Conclusion

In this article the following results are obtain:

- Architecture of the remote controlled system has been proposed. It can be utilized for different development applications.
- Specific elements are suggested for the system building. The selected components parameters are in accordance with the system requirements.

Acknowledgement

This work was supported in part under grants of scientific research project by NIS №172ПД0008-07 (session 2017-2018) and Faculty of Telecommunications, Technical University of Sofia.

REFERENCES

[1] Iszaidy, I., A. Alias, R. Ngadiran, R.B. Ahmad, M.I. Jais, D. Shuhaizar Video size comparison for embedded vehicle speed detection & travel time estimation system by using Raspberry Pi. Proceedings of International Conference on Robotics, Automation and Sciences, ICORAS 2016, art. No. 7872631. 2016, pp 196-203.

[2] Raspberry Pi NoIR Camera v2. http://www.farnell.com/datasheets/2056180.pdf

[3] Raspberry Pi 3 Model B. https://cdn.sparkfun.com/datasheets/Dev/RaspberryPi/2020826.pdf.

[4] SDIO101A, SD/SDIO/MMC/CE-ATA host controller. http://www.nxp.com/documents/data_sheet/SDIO101A.pdf

[5] Sahani, M., M.N. Mohanty, Realization of Different Algorithms Using Raspberry Pi for Real-Time Image Processing Application. Advances in Intelligent Systems and Computing, 309 AISC, Vol. 2, 2015, pp. 473-479.

Assoc. Prof. Dr. Ivo N. Dochev *– works in Technical University of Sofia. He received the M. Sc. (Dipl. Ing.) degree in electrical engineering from Technical University of Sofia, Bulgaria, in 1996. In 1996 he joined the Faculty of Telecommunications and Technology, Technical University of Sofia, where he is currently working on topics in measure in telecommunications. He received the Ph. D. degree, in 2009. From 2010 he is Associate Professor in Faculty of Telecommunications, Technical University of Sofia. He has scientific interests in the area of measurement in telecommunications, electromagnetic compatible and analog circuit design.*

e-mail: idochev@tu-sofia.bg

Assoc. Prof. Dr. Liljana E. Docheva *– works in Technical University of Sofia. She received the M. Sc. (Dipl. Ing.) degree in electrical engineering from Technical University of Sofia, Bulgaria, in 1996. In 2006 she joined the Faculty of Telecommunications and Technology, Technical University of Sofia, where she is currently working on topics in television systems. She received the Ph. D. degree, in 2009. From 2015 she is Associate Professor in Faculty of Telecommunications, Technical University of Sofia. She has scientific interests in the area of television systems, image processing and neural networks.*

e-mail: docheva@tu-sofia.bg

Eng. Maria Tz. Pavlova *works in Technical University of Sofia as a senior assistant since 2017 where she is currently working on topics in measure in telecommunications.*

e-mail: mariapavlova@tu-sofia.bg

Received on: 28.05.2018

CBIR with dual tree complex wavelet transform using maximally flat all-pass filter

Stella Vetova, Ivo Draganov, Ivan Ivanov

In the following paper linear-phase filters for Dual-Tree Complex Wavelet Transform implementation based on all-pass filter synthesis with maximally flat characteristics is proposed. This transform is a part of already presented content-based image retrieval algorithm with local features, using Hausdorff distance. It is based on the image division (8x8) from which local features are extracted through the Dual-Tree Complex Wavelet Transform, respectively feature vectors built. Then, we compare its experiment results with the ones of other three algorithms based on both local or global features and the Dual-Tree Complex Wavelet Transform. The used distance measures are Hausdorff distance and Euclidean distance. From the four discussed algorithms the proposed one has the best Precision results because of the vectors formed on the base of the local position of the details and the use of Hausdorff distance. The accomplished experiments show that this algorithm successfully detects details, shape and texture between objects with sharp jumps in the intensity of the two dimensional signal.

Извличане на изображения по съдържание чрез Комплексно уейвлетно преобразуване с дуални дървета с използването на всепропускащи филтри с максимално гладки характеристики (С. М. Ветова, И. Р. Драганов, И. Д. Иванов). *В настоящия доклад са предложени линейно-фазови филтри за внедряване на Комплексно уейвлетно преобразуване с дуални дървета, базирано на всепропускащи филтри с максимално гладки характеристики. Тази трансформация е част от вече представен алгоритъм за съдържателно извличане на характеристики с използването на локални такива и разстояние на Хаусдорф. Той е проектиран на базата на разделянето на подизображения (8x8), от които се извличат локални характеристики чрез Комплексното уейвлетно преобразуване с дуални дървета и съответно се формират векторите от характеристики. Получените резултати са сравнени и анализирани с тези на други алгоритми, базирани на локални или глобални характеристики и същото преобразуване. Използваните метрики за подобие са разстояние на Хаусдорф и Евклидово разстояние. От четирите алгоритъма предложеният се отличава с най-добри резултати по отношение на ефективност, тъй като векторите от характеристики са генерирани на базата на локалното разположение на детайлите. Проведените изследвания показват, че разработеният алгоритъм успешно разпознава детайли, форма и текстура между обекти с остри скокове в интензитета.*

Introduction

The Wavelet Transform is a technique for image representation through spatial and frequency features. The transform analyses the image through multiscale constructions in low computational cost and high speed.

Taking account of these advantages, a great number of researchers design and propose wavelet transform based algorithms.

The usage of the wavelet transform technique may be classified into three groups: for primitives feature extraction, for statistics data computation and for reducing the size of the feature vector.

Thus, for a primitive feature extraction Bhat and Sundaraguru [1] propose a CBIR algorithm for texture features combining wavelet transform and Local Binary Pattern (LBP) to achieve a rotation normalization method using the circular shift of the feature.

Krishna, Sirisha and Mdhavi [2] propose another algorithm for texture extraction, dividing an image into "blocks" and obtaining their features apply the Discrete Wavelet Transform.

To extract shape features, Vijendran and Kumar [3] design an algorithm, combining the Discrete Wavelet Transform and the Histogram Oriented Gradient. Their purpose is to describe a 16x16 pixel region of a preliminarily calculated interest point.

For combined primitives features extraction, most often authors propose methods for texture and color feature extraction.

In [4] Hossain and Islam design a CBIR method using the Discrete Wavelet Transform and Gabor wavelet transform. They calculate mean and standard coefficient on the base of the previously calculated wavelet ones, using the first transform. Then, they apply the second one to generate feature vector under each scale and orientation and combine the result features of the two transforms. In addition, they add the color feature vector generated, using HSV histogram, autocorrelogram and color moment and achieve a 1x190 feature vector. As a result, the algorithm reaches retrieval speed of 1,385586 sec.

Although the wide usage of Gabor wavelet transform, the orientation and scales on the precision rate of the CBIR are not included in the CBIR algorithms design [5]. That's why, Said and Khurshid [5] apply Gabor wavelet transform, color correlogram, HSV histogram, the effect of varying the number of scales and orientations in Gabor texture for color and texture features vectors generation.

In [6] the authors propose a new algorithm for texture and color features. They catch the primitives using respectively the wavelet transform and the color histogram. For each R, G and B component of a RGB image the color histogram is generated and then the transform executed.

Similarly, in [7] the authors use RGB images and they transform the RGB color space into three subsets and apply segmentation. For each segment they obtain color features through dominant color descriptor (DCD), histogram and statistic components. To extract texture features, the authors propose wavelet transform for wavelet coefficient computation for the entire image. The final feature vector includes the features from the segmentation and the ones obtained on the base of the entire image.

To build algorithms for feature extraction for the three basic primitives (color, texture and shape), Pandey and Kushwah [8] combine color coding (CC) for color, Hu moments for shape and both Gray Level Difference Method (GLDM) and the Discrete Wavelet Transform for texture features extraction. Thus, they achieve a rotation, scaling and translation resistant feature vectors.

In [9] Gupta and his research team propose another CBIR algorithm. They use the Discrete Wavelet Transform for texture analysis, the Dominant Color Descriptor (DCD) for color and Hough Transform for shape feature extraction.

Using the wavelet transform for statistics data computation, Giveki and colleagues [10] design an algorithm for color features extraction. To this end, they convert the RGB images into Lab color space and then they extract the features of each of the color channels, using wavelet transform. As a result, they generate a feature vector on the base of the first and second order moments of the wavelet coefficients.

Similarly, in [11] the authors design another CBIR algorithm for color features extraction where Red, Green and Blue components are extracted from RGB images and then 2D Haar wavelet transform is executed on each of the color matrices.

In order to generate feature vectors with small size, other authors apply the wavelet transform to reduce the size. Thus, Patel and Jerpude [12] convert the RGB image into YCbCr color space since Y component contains grey scale information and the other two the color one. They use Canny edge detection on the Y component for edge detection and build the color histogram on the R, G and B components. To reduce the size of the achieved feature vector, Haar wavelet transform is used.

According to another classification for the wavelet transform usage, the transform may be applied on the entire image [1], [3], [4], [5], [6], [7], [8], [9], [10], [11], [12] or on its segments [2], [7].

In the presented report, we propose a CBIR, using 8x8 division of the image. Local features are extracted from the subimages and the feature vectors are built. We estimate and compare the work of four different algorithms, using local or global features and Hausdorff distance and Euclidean distance as a distance measure.

Method

The Dual-Tree Complex Wavelet Transform (DT CWT) is designed in 1998 by Nick Kingsbury. Its construction uses one binary wavelet tree for the real part and another one for the imaginary part of the Complex Transform, both consisting of highpass and lowpass filters. The Discrete Wavelet Transform is performed on each of the trees. Thus, DT CWT produces an analytic signal with the following

properties: smooth non-oscillating magnitude; nearly shift-invariant magnitude; significantly reduced aliasing effect; directional wavelets in higher dimensions.

Using the transform each finite-energy analog signal *x(t)* [13] is decomposed on the base of wavelets and scaling functions via:

$$x(t) = \sum_{n=-\infty}^{\infty} c(n)\phi(t-n) + \sum_{j=0}^{\infty}\sum_{n=-\infty}^{\infty} d(j,n)2^{j/2}\psi(2^j t - n) \quad (1)$$

where *c(n)* – scaling coefficients; *d(j,n)* – wavelet coefficients. Both are computed via the inner products (2) and (3) as follows:

$$c(n) = \int_{-\infty}^{\infty} x(t)\phi(t-n)dt \quad (2)$$

$$d(j,n) = 2^{j/2}\int_{-\infty}^{\infty} x(t)\psi(2^j t - n)dt \quad (3)$$

Both types of coefficients provide a time-frequency analysis of the signal by measuring its frequency content at different times [13].

The wavelet coefficients consist of samples of the step response of the wavelet

$$d(j,n) \approx 2^{-3j/2}\Delta \int_{-\infty}^{2^j t_0 - n} \psi(t)dt \quad (4)$$

where Δ - height of the jump; $\psi(t)$ - bandpass function that oscillates around zero; *d(j,n)* – function of *n*; the factor 2^j in the upper limit ($j \geq 0$) amplifies the sensitivity of *d(j,n)* to the time shift t_0.

DT CWT is a biorthogonal transform, which uses linear-phase filters, satisfying the Perfect Reconstruction (PR) condition [8] and which produces approximately analytic signal:

$$\Psi(t) := \Psi_R(t) + j\Psi_J(t) \quad (5)$$

where $\Psi_R(t)$ and $\Psi_J(t)$ are the wavelets generated by the two Discrete Wavelet Transforms (DWTs).

In order to reach a nearly shift-invariant wavelet transform, one of the two lowpass filters has to be nearly half-sample shift to the other:

$$J_0(k) \approx R_0(k-0.5) \Rightarrow \Psi_J(t) \approx H\{\Psi_R(t)\} \quad (6)$$

DT CWT has 2D DT CWT extension for two-dimensional signal analysis. This version produces oriented wavelets and approximately analytic signal. To this end, it uses the following six real and six imaginary wavelets:

For -45° oriented wavelets:

$$Real\,Part\{\psi(x,y)\} = \psi_h(x)\psi_h(y) - \psi_g(x)\psi_g(y) \quad (7)$$

$$Imag\,Part\{\psi(x,y)\} = \psi_g(x)\psi_h(y) + \psi_h(x)\psi_g(y) \quad (8)$$

For +45° oriented wavelets:

$$Real\,Part\{\psi(x,y)\} = \psi_h(x)\psi_h(y) + \psi_g(x)\psi_g(y) \quad (9)$$

$$Imag\,Part\{\psi(x,y)\} = \psi_g(x)\psi_h(y) - \psi_h(x)\psi_g(y) \quad (10)$$

For -15° oriented wavelets:

$$Real\,Part\{\psi(x,y)\} = \phi_h(x)\psi_h(y) - \phi_g(x)\psi_g(y) \quad (11)$$

$$Imag\,Part\{\psi(x,y)\} = \phi_h(x)\psi_g(y) + \phi_g(x)\psi_h(y) \quad (12)$$

For +15° oriented wavelets:

$$Real\,Part\{\psi(x,y)\} = \phi_h(x)\psi_h(y) + \phi_g(x)\psi_g(y) \quad (13)$$

$$Imag\,Part\{\psi(x,y)\} = \phi_h(x)\psi_g(y) - \phi_g(x)\psi_h(y) \quad (14)$$

For -75° oriented wavelets:

$$Real\,Part\{\psi(x,y)\} = \psi_h(x)\phi_h(y) - \psi_g(x)\phi_g(y) \quad (15)$$

$$Imag\,Part\{\psi(x,y)\} = \psi_g(x)\phi_h(y) + \psi_h(x)\phi_g(y) \ldots (16)$$

For +75° oriented wavelets:

$$Real\,Part\{\psi(x,y)\} = \psi_h(x)\phi_h(y) + \psi_g(x)\phi_g(y) \quad (17)$$

$$Imag\,Part\{\psi(x,y)\} = \psi_g(x)\phi_h(y) - \psi_h(x)\phi_g(y) \quad (18)$$

In order to implement all the oriented wavelet (7) - (18) we consider the use of linear-phase filters as essential part of DT CWT. They need to be based on the all-pass filters with maximally flat characteristics. Their design is presented on Fig. 1 through block diagram, illustrating the process of the coefficient computation by steps.

Algorithm

Several parameters take part in the design of the all-pass filters as follows: *K, L* - flatness parameters; *d*-delay; *$A_1(z)$, $A_2(z)$* – transfer functions of the all-pass filters returned by the algorithm represented by denominators $\vec{a_1}, \vec{a_2}$; *K+L* – filter degree; $\vec{p}, \vec{q}$ - parameters which represent the total low-pass response. The frequency response magnitude has a flat characteristic at $w = 0$ and $w = \pi$ [14].

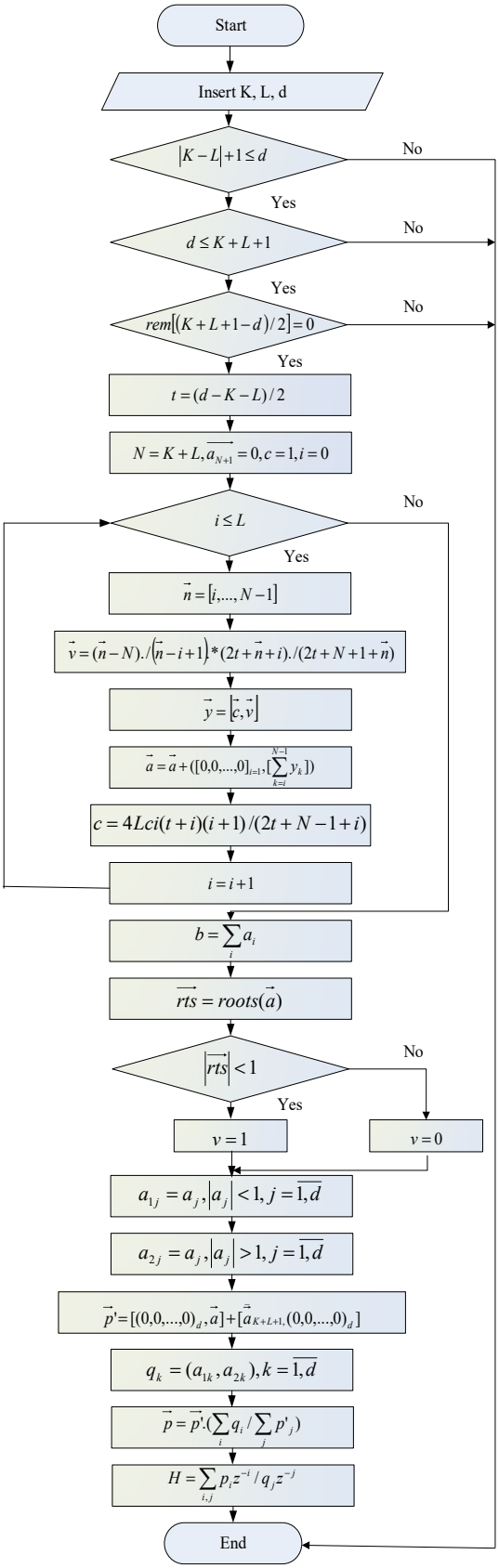

Fig. 1. Block diagram of the all-pass filters with maximally flat characteristics.

Used Data

For the purpose of the accomplished experiments, Wang image test database [15], containing 1000 RGB images, was used. The images are classified into 10 groups: "Nature", "Architecture", "Vehicles", "Dinosaurs", "Elephants", "Flowers", "Horses", "Food", "Africa" and "Social life". They are distinguished for size of 256 x 384 px and 384 x 256 px in JPEG format.

Results

The purpose of the following experiments is to estimate the efficiency of four algorithms [16] and accomplish comparative analysis between them. The first two of them, the Algorithm with Local Features, using Hausdorff distance (ALFH) and the Algorithm with Local Features, using Euclidean distance (ALFE) are built on the base of local features extracted from 64 subimages (8x8). The other two, the Algorithm with Global Features, using Hausdorff distance and the Algorithm with Global Features, using Euclidean distance, use global features of the images.

The presented four algorithms have close Precision values (Precision and Recall are used as efficiency measures as defined in [16]) in different number of the submitted query-images. ALFH presents the best results. ALFE demonstrates close to the ALFH ones in the area of thirty query-images where ALFH Precision has a slight decrease caused by the accumulation of results with lower values. From the group of the global features, AGFE retrieves results with higher Precision and in the list of the four algorithms it takes the third place. Fig. 2 shows the advantage of the algorithms, using local features which is caused by the fact that their vectors are based on the local position of the details.

The four algorithms alter their Recall results increasing the query-image number (Fig. 3). As they increase, the ALFE Recall results gradually decrease and for the AGFE ones, it is the smallest with a tendency towards increasing. The AGFH Recall values sharply decrease and then demonstrate values close to the ones of the rest three algorithms. Reaching the maximum number of tested query-images (50), it has the highest Recall result. On the other hand, ALFH is notable for its tendency to increase and in fifty query-images it takes the second place. AGFH retrieves the greatest number of relevant and irrelevant images and ALFH retrieves less than it. The least number of images from these two groups in fifty query-images are retrieved by AGFE.

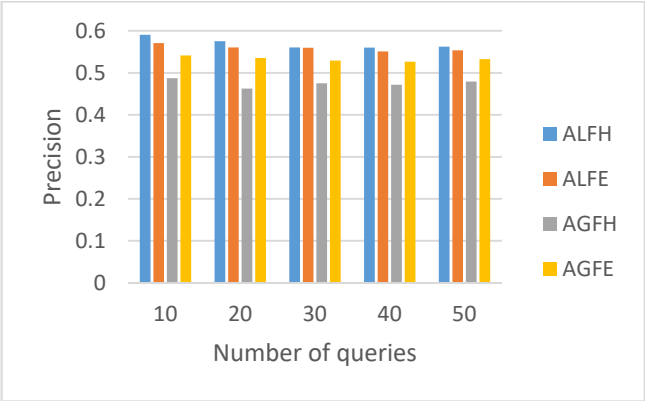

Fig. 2. Precision against number of queries for ALFH, ALFE, AGFH, AGFE.

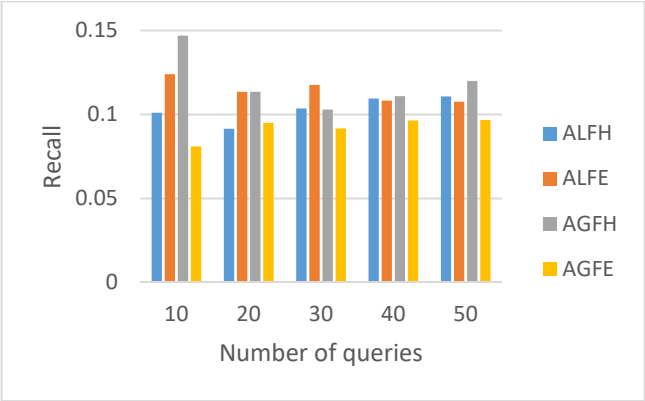

Fig. 3. Recall against number of queries for ALFH, ALFE, AGFH, AGFE.

The Averaged Normalized Modified Retrieval Rank (ANMRR) [16] comparison on Fig. 4 shows that AGFH retrieves the greatest number of irrelevant images followed by ALFE. ALFH and AGFE have close and the lowest ANMRRvalues. This highlights their ability to retrieve less irrelevant images and leads to greater efficiency than the other two algorithms.

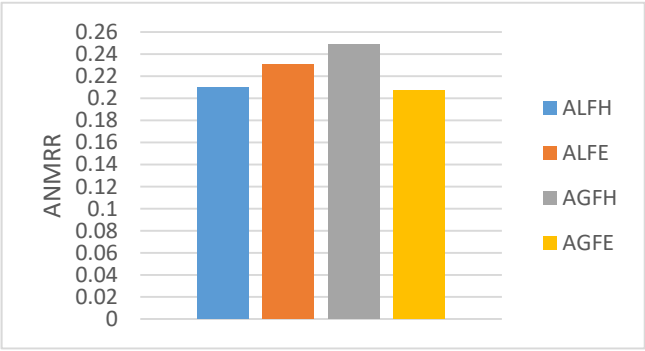

Fig. 4. Efficiency bar chart according to ANMRR.

A result retrieved by ALFH is presented on Fig. 5. For the purpose, a query-image from the group "Africa" which is listed in the first position in the sequence of images and outlined in black border is submitted. The result indicates that ALFH has the ability to detect details, shape and texture. It takes account of the homogeneous areas and the transitions between areas with sharp jumps in the intensity of the two dimensional signal. As a result, images similar to the query in respect to smooth and sharp jumps are retrieved. The images with ranks 1, 2, 3, 4, 6, 7 and 8 have sharp transitions from lower to higher intensity values. Thus, ALFH detects the shape, texture and details retrieving relevant images by these primitives. The slight semantic relevance of the images to the query-image and the differences on color are the shortcomings of the retrieved result to work upon in future.

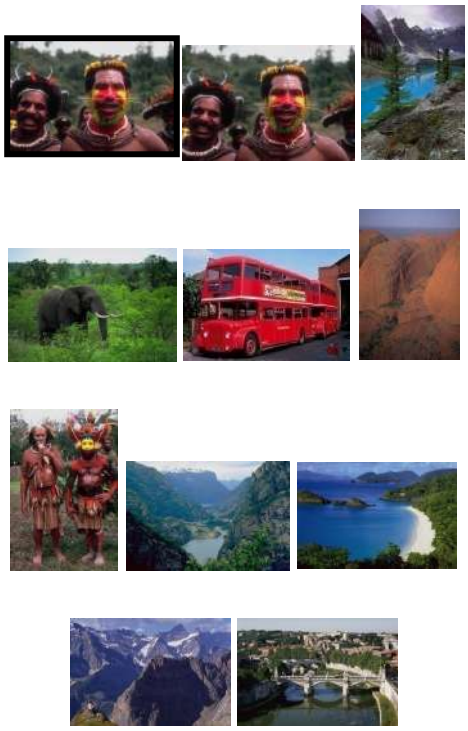

Fig. 5. Images in order of retrieval for the query in black frame from category "Africa" for ALFH.

Fig. 6 presents a sequence of images retrieved for the submitted query-image from the category "Social life". It concerns the image detection on the base of the location of the objects relative to one another by intensity. The alternation of the homogeneous areas with close intensity values figuring borders and shapes out for the similarity computation is highlighted. The retrieved result has better semantic relevance (50%) than the result presented on Fig. 5.

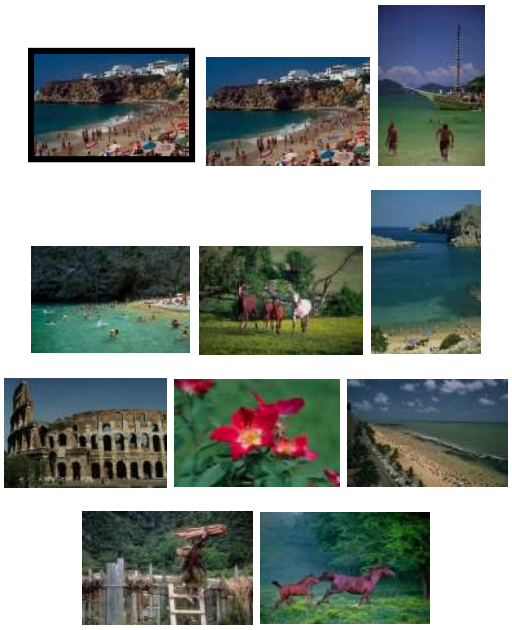

Fig. 6. Images in order of retrieval for the query in black frame from category "Social life" for ALFH.

For the submitted query-image from the category "Food" (Fig. 7) ALFH retrieves images, detected as similar on the base of the spatial location of the objects and their shape.

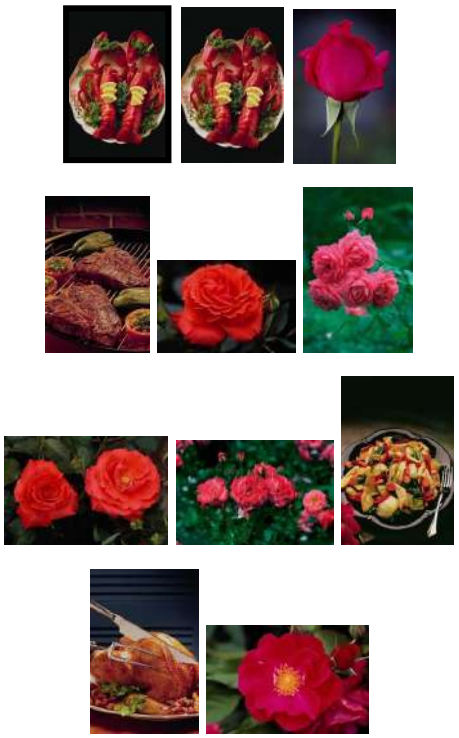

Fig. 7. Images in order of retrieval for the query in black frame from category "Food" for ALFH.

The small by size and regularly repeated by structure shapes with equal directionality, complexion and contrast define the primitive texture. Thus, ALFH demonstrates the ability to retrieve similar images by texture. The result for the discussed category reaches detection on semantics for 40%.

Conclusion

From the four discussed algorithms ALFH has the best Precision results because of the vectors formed on the base of the local position of the details and the use of Hausdorff distance which takes account of the details of the shape.

On the other hand, ALFH takes the second position in the list of the number of retrieved images. Nevertheless, it has the best ratio of number of relevant retrieved images to the total number of retrieved images which causes the highest Precision values for this algorithm.

The accomplished experiments show that the designed ALFH successfully detects details, shape and texture between objects with sharp jumps in the intensity of the two dimensional signal. Besides, ALFH has the ability to detect homogeneous areas with close intensity which figures borders and shapes out.

REFERENCES

[1] Bhat, Sh., R. Sundaraguru. Effective Analysis of Image Retrieval Using Wavelet Transform and Local Binary Pattern, International Journal of Advance Electrical and Electronics Engineering, Volume: 6 Issue: 1_2, 2017, pages 200-204.

[2] Krishna, J., T. Sirisha, V. Madhavi. Image Retrieval based on Texture using Various Discrete Wavelet Transform Sub Bands, National Conference on Emerging Trends in Computing, 2017, pages 22-24.

[3] Vijendran, A., S. Kumar. A New Content Based Image Retrieval System by HOG of Wavelet Sub Bands, International Journal of Signal Processing, Image Processing and Pattern Recognition, Vol. 8, No. 4, 2015, pages. 297-306.

[4] Hossain, Sh., R. Islam. A New Approach of Content Based Image Retrieval, Using Color and Texture Features, British Journal of Applied Science & Technology, Volume: 21(3), 2017, pages 1-16.

[5] Said, L., K. Khurshid. An Efficient Content Based Image Retrieval Systemand the Selecting Optimal Orientations of Gabor Wavelet for CBIR System, Gomal University Journal of Research, Vol. 33, Issue 2, DEC 2017, pages 26-34.

[6] Kamaraji, M., V. Savitha. Content Based Imge Retrieval using Wavelet Transforms with Dynamic Texture

(DT), Proceedings of IISTEM International Conference, 2017, pages 44-47.

[7] Rashno, A., S. Sadri. Content-based Image Retrieval with Color and Texture Features in Neutrosophic Domain, 3rd International Conference on Pattern Recognition and Image Analysis, 2017, pages 50-55.

[8] Pandey, D., Sh. Kushwah. An Efficient Low Level Features of CBIR using Wavelet, GLDM and SMOSVM Method, International Journal of Signal Processing, Image Processing and Pattern Recognition, Vol. 10, No. 3, 2017, pages 13-22.

[9] Gupta, G., M. Dixit. CBIR on Biometric Application using Hough Transform with DCD ,DWT Features and SVM Classification, International Journal of Engineering and Innovative Technology, Volume: 5, Issue: 12, 2016, pages 46-50.

[10] Giveki, D., A. Soltanshahi, F. Shiri, H. Tarrah. A New Content Based Image Retrieval Model Based on Wavelet Transform, Journal of Computer and Communications, Volume:3, 2015, pages 66-73.

[11] Gunjal S., S. Rokade. An Efficient Technique For Content Based Image Retrieval Using Haar Wavelet Transform, International Journal of Informative & Futuristic Research, Volume: 2, Issue: 11, 2015, pages 4110-4117.

[12] Patel, D., A. Yerpude. Content Based Image Retrieval using Color Edge Detection and Haar Wavelet Transform, International Research Journal of Engineering and Technology, Volume: 2 Issue: 9, 2015, pages 1906-1911.

[13] Selesnick, I., R. Baraniuk, N. Kingsbur. The Dual-Tree Complex Wavelet Transform, IEEE Signal Processing Magazine, 2005, pp. 123-151.

[14] Selesnick, I. Low-Pass Filters Realizable as All-Pass Sums: Design via a New Flat Delay Filter, IEEE Transactions on Circuits and Systems – II: Analog and Digital Signal Processing, Vol. 46, No.1, 1999, pp. 40-50.

[15] Wang, J., J. Li, G. Wiederhold, SIMPLIcity: Semantics-sensitive Integrated Matching for Picture LIbraries, IEEE Transactions on Pattern Analysis and Machine Intelligence, vol 23, no.9,2001, pp. 947-963.

[16] Vetova, St., I. Draganov, I. Ivanov, V. Mladenov. CBIR Efficiency Enhancement using Local Features Algorithm with Hausdorff Disance, European Conference on Electrical Engineering and Computer Science, Volume 5, 2017, pp. 116-123.

Eng. Stella M. Vetova *graduated the Faculty of Computer Systems in the Technical University of Sofia. Her work concerns databases, image databases, image recognition, artificial intelligence.*

Tel:+359 2 965 2274 e-mail: vetova.bas@gmail.com

Assoc. Prof. Dr. Ivo R. Draganov *is with the Faculty of Telecommunications in Technical University of Sofia, Bulgaria. His scientific interests are in the areas of digital image processing, pattern recognition and neural networks.*

tel.:+359 2 965 2274 e-mail: idraganov@tu-sofia.bg

Dr. Ivan D. Ivanov *graduated the Faculty of Telecommunications in the Technical University of Sofia. His scientific work is in the field of information and network security as well as databases security.*

tel.:+359 2 80 62 234 e-mail:i.ivanov@utp.bg

Received on: 16.02.2018

Construction of a preliminary educational system for file backup system using secret sharing technique

Takeshi Tanaka, Nobuharu Okamitsu, Noriyuki Yamada, Toyoharu Takemoto, Katia Vutova

Information-Technology Promotion Agency points out Ransomware as the second-ranked damage to organizations as well as individuals in "10 Major Security Threats 2017". Information is stored in three data files separately by using the secret sharing technology that can freeze the activities of Ransomware. When two of three distributed files are combined, the original information can be reproduced. We have built a preliminary education system for file backup using secret sharing technique to study the outline of this technology and experience operation. In the future, as an application of this technology, we would like to build a high secure information environment at home where you can fulfill the educational oriented work safely. In the environment, you are unnecessary to bring back the USB memory to your home. Also, we will try to use "Secure Explorer" technology to promote "work style reform" at the educational fields.

Keywords – back up, educational system, information security, ransomeware, sectret sharing technology.

Изграждане на тестова система за архивиране на файлове в сферата на образованието на базата на „secret sharing" технология (Такеши Танака, Нобухару Окамитсу, Нориюки Ямада, Тойохару Такемото, Катя Ж. Вутова). *Агенцията за насърчаване на информационните технологии NIPA (National IT Promotion Agency - Republic of Korea) посочва Ransomware като втори по значимост зловреден вирус за организации и отделни потрбители в материала "10-те най-големи заплахи за сигурността - 2017". В използваната от нас и описана в тази статия система, информацията се съхранява отделно в три файла с данни, като се използва технологията "secret sharing (тайно споделяне)", която може да блокира дейността на Ransomware вируса. Когато се комбинират два от трите разпределени файла, оригиналната информация може да бъде възпроизведена. Инсталирахме опитна версия на предлаганата „secret sharing" технология за целите на образованието в Хирошимски технологичен институт като част от система за архивиране на файлове - "Secure Explorer". Целта е да се изучат по-подробно практическите плюсове и минуси на тази технология и придобиването на повече опит при нейното използване в практиката. В бъдеще, като приложение на "secret sharing" технологията, бихме искали да изградим сигурна информационна среда, където може да се разчита на целостта и безопасността на съхраняваната информация в съвременните IT условия, без да е необходимо да се използват и съхраняват отделни копия на външни носители, които да се носят в къщи. Също така ще се опитаме да използваме технологията "Secure Explorer", за да въведем и популяризираме тази нова "реформа в стила на работата" в сферата на образованието.*

1. Introduction

Information-Technology Promotion Agency points out Ransomware [1,2] as the second-ranked damage to organizations as well as individuals in "10 Major Security Threats 2017" [3].

One of secure and efficient key management mechanisms is secret sharing scheme that lets you split your secret into several parts and distribute them among selected parties. The secret can be recovered once these parties collaborate in some way.

Secret sharing schemes is one of the key management schemes or establishment schemes invented separately in 1979 by Shamir [4] and Blakley [5] as a solution to safeguard cryptographic keys. Secret sharing schemes are also used to protect other

types of secrets, such as a secret recipe, and etc. [6].

In this research, we report construction of a preliminary educational system for learning and operating file backup system using secret sharing technique. Information is stored in three data files separately utilizing secret sharing technology that can freeze the activities of Ransomware. Two of three data files are combined to reproduce the original information when it is necessary.

2. Characteristics of Secure Explorer

2.1. Summary of Secure Explorer

(a) Characteristic 1. Never be infected with unknown malware including Ransomware.

We utilize secret sharing (electronic sharing) and carry out sharing process at the moment of closing the file on Windows. Divided files in themselves do not have entities, so they don't be directly influenced even if they are infected with Ransomware (malware). If Ransomware (malware) can't act, hardware and networks will not be destroyed. We can also cope with unknown threats from now on.

(b) Characteristic 2. Guarantee security of cloud storage by making data meaningless.

Data divided by secret sharing (electronic sharing) technology has no meaning. Even if someone can get one divided piece, he can't read the original data from it even by using a supercomputer. Therefore, one piece lost doesn't mean information leakage.

(c) Characteristic 3. The system is simple and easy to use. Its operation is alike to Windows Explorer.

Operation and first setting are extremely simple. You can start on Windows Explorer screen and anyone can operate easily. In addition, you can flexibly change operational usage.

(d) Characteristic 4. Even if your PC is destroyed, you can reconstruct the original data using other PC.

All data is stored in three distributed storages [① main unit storage ② USB memory ③ cloud storage] by secret sharing technique. If you have two or more of the distributed data, you can restore the original data. Moreover, since it is possible to set up another additional storage, you can restore the data immediately even if your PC is destroyed by some virus or stolen.

2.2. Details of Secure Explorer

(a) Characteristic 1. Never be infected with unknown malware (including Ransomware).

Ransomware can be active on macro formats (exe), such as .doc, .docx, .docm, .xls, .xlsx, .xlsm, .ppt, .pptx, pptm, .pdf, .js, .lnk, and JavaScript files (.js), etc. Also malwares are often embedded in Microsoft Office applications (Word, Excel, etc.), PDF format files, or executable format (extension such as exe).

"Secure Explorer" exploits secret sharing (electronic sharing) technology and carries out dispersing process at the moment of closing the file on Windows – Fig.1.

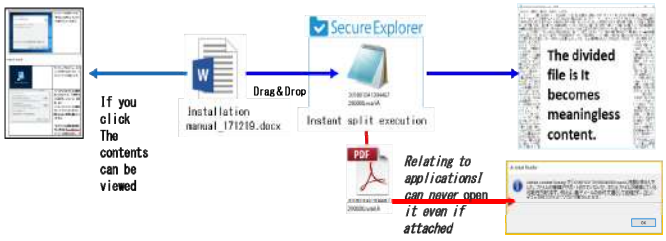

Fig.1. Action of "Secure Explorer".

Distributed files in themselves are binary data that is emulsified by mixed garbage and have no entity. And, these files can't be tied directly to any applications.

The divided bit-level array is different from original data's. So, our system will completely stop the activity of Ransomware (malware) taking place in macro formats (exe) and JavaScript. We can also cope with unknown threats from now on.

Under the attack of Ransomware (malware), the following serious task problems will emerge:

- Infrastructure is locked
- Important files can't be utilized
- Risks of information leakage
- Possibility to lose data by anti-virus software.

Destructive attack to information by Ransomware (malware) won't stand well in "Secure Explorer". When Ransomware attacks to one divided file, you can restore the original data completely by gathering the rest of the divided pieces.

This system dissolves the risk that important information is leaked to the outside by malware. Because data has become unimportant due to secret sharing, so even if a malicious third party gets the data, it is "not important = meaningless" information. It can't be analogized. It will not become information leakage.

There is a case where Ransomware (malware) may invade into divided files. However, these files have lost executable formats without reality, so they can't work by themselves.

Each divided file is binary data that is divided after mixing the original data with garbage, and can't be tied directly to the application. Because the array of the distributed bit-level is different from original data's, Ransomware (malware) in macros and JavaScript can't act.

When you click the file icon and carry out the restoration process, this system detects that the divided file has changed, and performs recovery processing (Fig.2). So the original file will be securely protected.

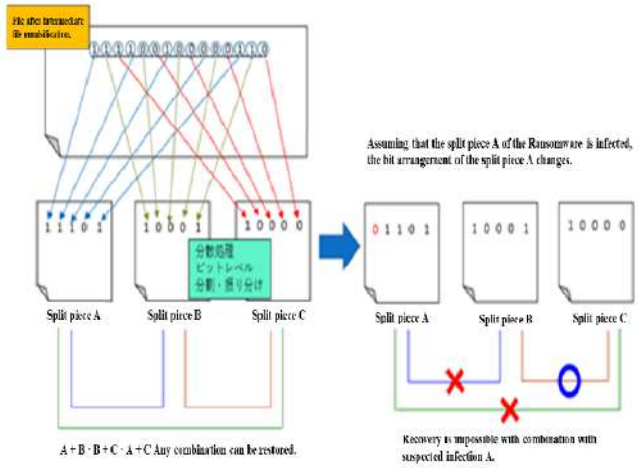

Fig.2. Operation (restoration) of "Secure Explorer".

(b) Characteristic 2. Make data meaningless and guarantee security of cloud storage.

This system divides the original information into several pieces and works in process not to be discerned the original data from each piece only. One piece includes part of the original information, but the amount of information of one distributed piece is insufficient, because its data is processed to not make sense.

Since it is kept secret by making "secret" information "disperse", it is named secret sharing. This technique is sometimes called "electronic sharing" (Fig.3).

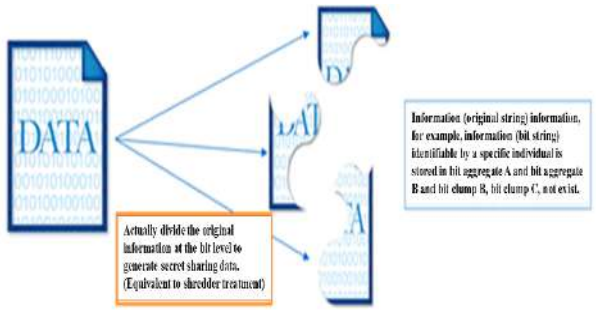

Fig.3. Image of electronic sharing.

The information is made up of bit strings of "0" and "1", whether it is a Word document, an Excel table or a Power Point presentation, or even a picture or an illustration.

When you apply the original application to files that only list “0” and “1”, you can get characters and images.

The most intuitive method is to extract each bit from the next. Neighboring bit string is not included in the same fragment of the former bit string.

By lacking information partially, you can’t analogize character strings or even characters.

If a bit string of the original file is multiplied by a random bit string, the original bit will become a completely different bit string. If you divide PDF file and divide its divided file again, emulsification processing is carried out, and all the binary information after the red line has be changed – Fig.4.

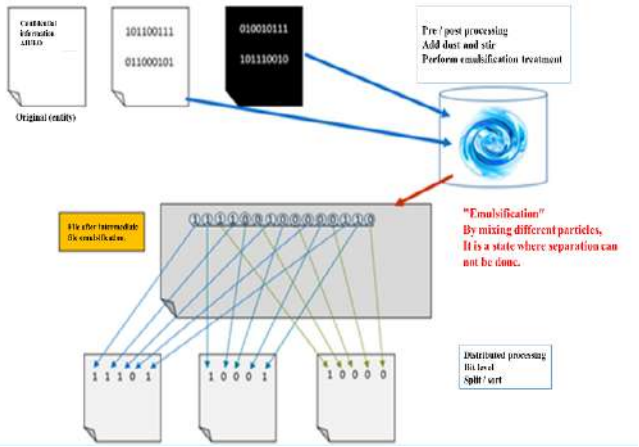

Fig.4. Secret sharing technology is an "emulsification".

In secret sharing, a random bit string is multiplied. Therefore, bit strings at first time are different from them at second time. When you file a data again, a different bit string from previous one has been completed.

Even if the divided pieces stored in the PC are stolen, you can restore the original data from other two pieces (Fig.5).

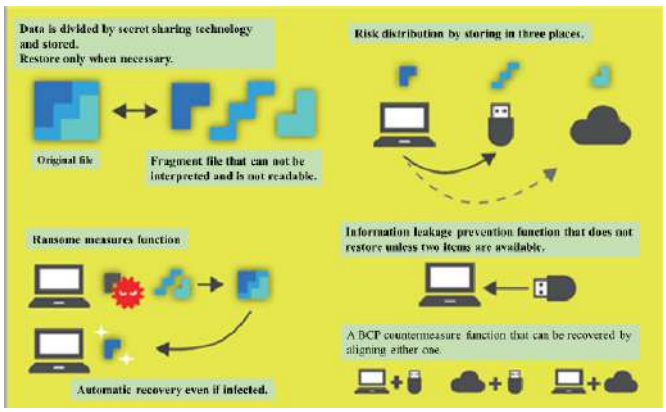

Fig.5. Image of electronic sharing (system).

After you did it, the stolen data doesn’t match with the divided pieces, and the restoration of the original data becomes absolutely impossible.

(c) Characteristic 3. Simple and easy to use under a familiar feeling of Windows Explorer operation.

Anyone can operate this system easily by reproducing the screen based on Windows Explorer.

After you only drag and drop files and folders to Secure Explorer, distributed processing is carried out by secret sharing engine (Figs.6-7).

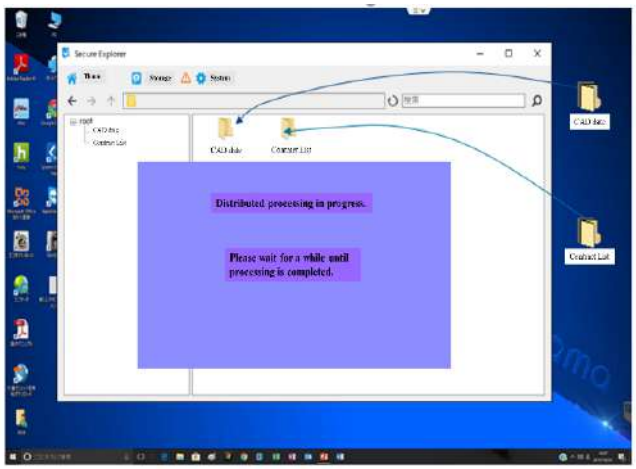

Fig.6. Screen based on Windows Explorer.

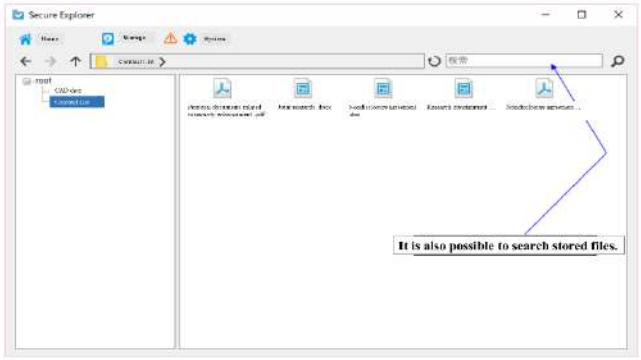

Fig.7. Screen based on Windows Explorer.

You can protect your important data from Ransomware (malware) and can also prevent information leakage.

If you will drug & drop all the files stored in the folder of contract list to "Secure Explorer", they are divided into 3 pieces by secret sharing technique and are stored immediately in three different storage destinations, respectively. When storage is completed, an icon with the same file name as the original data is displayed.

If you double-click on the collaborative research docx icon, the Word file is restored. The operation is the same as Windows Explorer, so you can use it immediately.

When you close the Microsoft Word file of the collaborative research which is now open, the redistribution processing is performed immediately (Fig.8). The divided files are kept in three storage places and the real file of Microsoft Word disappears from the main part of the personal computer. Since there is no real file, it is definitely not infected with malware typified by Ransomware.

- Never be infected by any type of unknown malware.

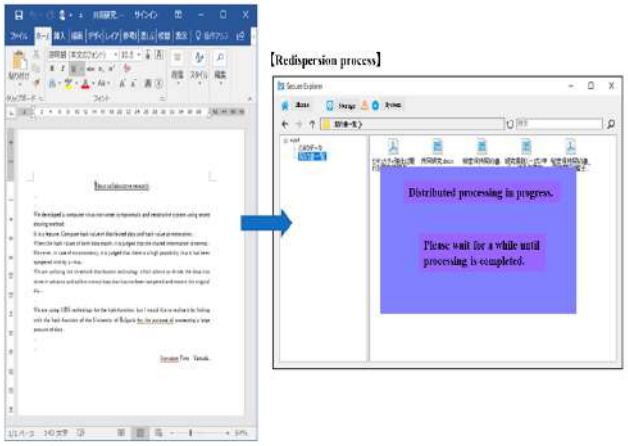

Fig.8. Image of distributed processing.

(d) Characteristic 4. Even if the PC is destroyed, other PC can restore the original file immediately.

- Secret sharing (threshold distribution) is ISO standardized technology that guarantees file security.

More than two piece-file are made by complete encryption utilizing physical random number of the same size as the original file. If the decryption key does not exist, the original file can be restored by arranging fixed number of piece. Since it can't be decoded from individual pieces alone, it is called information theoretical safety (Figs.9, 10).

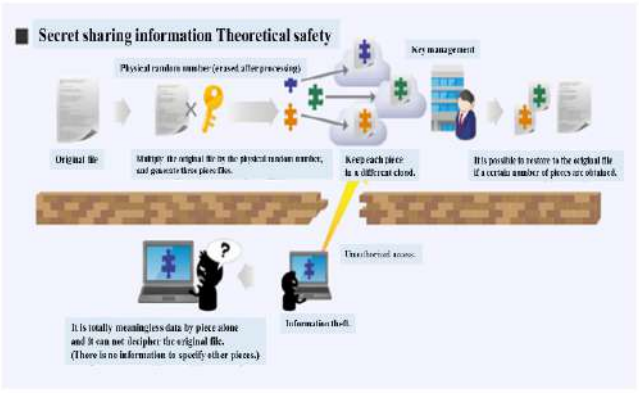

Fig.9. Schematic about the theoretical safety of secret sharing technology.

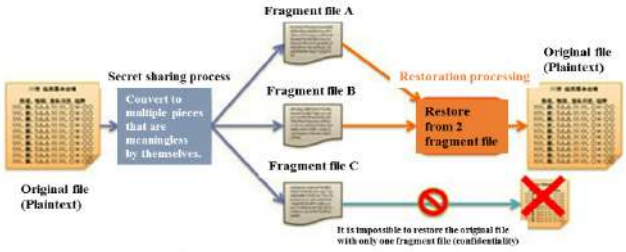

Fig.10. Example [7] of secret sharing that can be restored from two pieces.

Threshold sharing technology stops to restore the original data from one stolen piece by a third party.

When one of the divided pieces containing important information has fallen into the hands of a third party, the formal user has to restore the original file from the rest of divided pieces first, and then perform the re-division processing.

The threshold sharing technology makes it possible to restore the original file with the remaining divided pieces even if one divided piece is lost.

In order to restore the data, you think you have to gather up all the divided pieces. But, as this system gives redundancy to the data on the time of division, the original data can be restored by grounding on a part of tallied data.

ISO issued the international standard of secret sharing technology (ISO / IEC 19592-2: 2017) in October, 2017. In this standard, they have adopted following five secret sharing schemes. Our "Secure Explorer" adopts AIST's library (AIST: National Institute of Advanced Industrial Science and Technology) which is based on "5. Computational Additive secret Sharing Scheme".

1. Shamir secret Sharing Scheme
2. Ramp Shamir secret Sharing Scheme
3. Additive secret Sharing Scheme for general adversary structure
4. Replicated additive secret Sharing Scheme
5. Computational Additive secret Sharing Scheme.

The storage destination is (Fig.11):

(i) internal storage (storage of PC's hard disk and linked by network),

(ii) external storage (removable disk such as USB memory),

(iii) cloud storage.

Furthermore, it is possible to select (i)+(ii)+(iii) as spare storage.

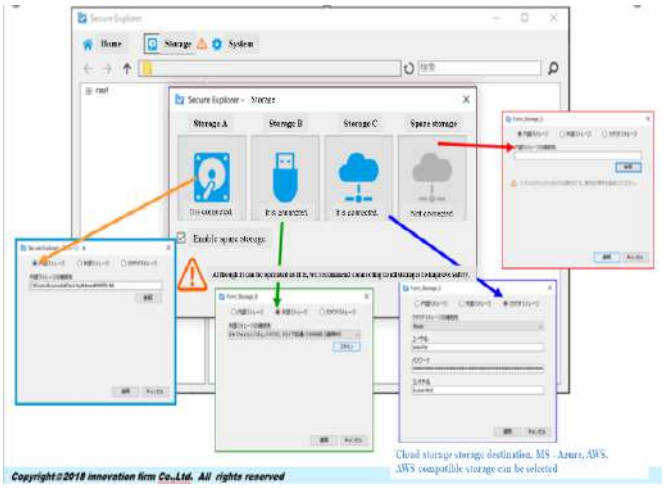

Fig.11. Image of storage destination.

The original information can never be analogized from pieces of data divided by secret sharing technique.

One divided piece of data contains only a part of the original data. It is impossible to restore the original data from it. Even had a third party got one of the divided pieces, they can't read any useful information from it.

(e) Characteristic 5. You can make the most of distinct features in your data center.

In the data center, the access record is always filed. So, you can check up on whether the divided pieces have been gathered or not. If someone gathered them, he was suspected of taking out them. If not, information has not been carried out.

Secret sharing technology is assumed to be used as a technology to support the data center or to preserve the cloud circumstances.

We are considering depositing the divided pieces into several data centers separately.

We are convinced of strict management of the divided pieces, because every data center has furnished the facility about severe preservation of data, and hackers are probably unable to hack many data centers at once.

3. Comparison with backup products and construction of information security

General backup products do not take countermeasures against malware such as Ransom as usual. In these cases, the infected file will be backed up without noticing an infection or a threat.

"Secure Explorer" performs distribution process of the secret sharing method at the moment of closing the file (data), and it can build up a definite form that guards against infection of malware.

In this form, uninfected divided pieces do to overwrite and renew a file (data) that fells under suspicion for invasion.

So, this system is always possible to maintain a safe situation.

Our preliminary educational system includes the following steps:

- Description of information security.
- Explanation of file backup system using secret sharing technique.
- Setting up and utilizing file backup system using secret sharing technique.
- Educational effect (operational experience etc.).

4. Summary

The characteristics of "Secure Explorer" in details and the merits of its utilizing are presented and discussed. Comparison with backup products and the steps in construction of information security are also presented.

We ensure data integrity by giving redundancy to each divided piece.

By adding redundant data such as so-called parity (RAID 5) to each divided piece, you can restore the original data from two of three divided pieces.

Even if one piece is missing or stolen, the original data can be restored from the remaining pieces.

Since information can't be analogized from lost divided pieces and original data can be restored from the remaining divided pieces, you can ensure business continuity without any troubles.

In the future, as an application of this technology, we would like to build a high secure information environment at home where you can fulfill the educational oriented work safely. In the environment, you are unnecessary to bring back the USB memory to your home.

Also, we will try to use "Secure Explorer" technology to promote "work style reform" at the educational fields.

5. Acknowledgments

At present, we express our thanks to the fact that empirical research of "Secure Explorer" is scheduled in some institutions such as Hiroshima Institute of Technology, Hiroshima International University, and National Ariake Technical College. The Agreement for Academic Cooperation and Exchange (2018-2023) between the Hiroshima Institute of Technology, Hiroshima, Japan and the Institute of electronics, Bulgarian Academy of Sciences, Sofia, Bulgaria is also acknowledged (by the authors T.Tanaka and K.Vutova).

REFERENCES

[1] https://www.trendmicro.com/ja_jp/security-intelligence/research-reports/threat-solution/ransomware.htm

[2] https://www.npa.go.jp/cyber/ransom/index.html

[3] https://www.ipa.go.jp/security/vuln/10threats2017.html

[4] Shamir, A. How to share a secret. Communications of the ACM, Vol. 22, No. 11, 1979, pp.612-613.

[5] Blakley, G.R. Safeguarding cryptographic keys. Proc. AFIPS 1979 National Computer Conference, New York, Vol. 48, 1979, pp.313-317.

[6] Ebri, N. Al, J. Baek, Ch. Y. Yeun. Study on Secret Sharing Schemes (SSS) and their applications. Proc. 2011 Int. Conf. for Internet Technology and Secured Transactions (ICITST), Abu Dhabi, United Arab Emirates, IEEE Xplore: February 2012, pp.40-45.

[7] http://www.ntt.co.jp/news2017/1710/171023a.html

Prof. Dr. Takeshi Tanaka *– Department of Electronics and Computer Engineering, Faculty of Engineering, Hiroshima Institute of Technology, 2-1-1, Miyake, Saeki-ku, Hiroshima, 731-5193, Japan.*

tel.+81-82-921-3121

e-mail: tanaka@cc.it-hiroshima.ac.jp

Mr. Nobuharu Okamitsu *Dr course student, Major in Intelligent Structure and Functional Science, Graduate School of Science and Technology, Hiroshima Institute of Technology, 2-1-1, Miyake, Saeki-ku, Hiroshima, 731-5193, Japan.*

tel.+81-82-921-3121 e-mail: n.okamitsu@nifty.com

Mr. Noriyuki Yamada *- Innovation Firm Co., Ltd, Taiyo Building 3F, 1-12-4, Iwamoto-cho, Chiyoda-ku, Tokyo 101-0032, Japan.*

tel.+81-3-5823-4398

e-mail: noriyuki.yamada@innov-firm.co.jp

Mr. Toyoharu Takemoto *– MIURA CORPORATION, 3-9, Minamisendahigashi, Naka-ku, Hiroshima 730-0054, Japan*

tel.+81-82-246-1155

Prof. DSc. Katia Zh. Vutova *– Head of Laboratory "Physical problems of electron beam technologies", Institute of Electronics, Bulgarian Academy of Sciences, 72 Tzarigradsko shosse blvd., 1784 Sofia, Bulgaria*

tel: +359-2-9795900 e-mail: katia@van-computers.com

Received on: 21.03.2018

ЕЛЕКТРОТЕХНИКА И ЕЛЕКТРОНИКА E+E

53 год. 11-12/2018

Научно-техническо списание

Издание на: **Съюза по електроника, електротехника и съобщения /CEEC/**

Адрес:
ул. "Раковски" № 108
ет. 5, стая 506
София 1000
тел.: +359 2 987 97 67
e-mail: epluse@mail.bg
http://epluse.fnts.bg

ISSN 0861-4717

С Ъ Д Ъ Р Ж А Н И Е

През 2018 г. списание Electrotechnica & Electronica се издава с финансовата подкрепа на фонд „Научни изследвания" към Министерството на образованието и науката.

UNION OF ELECTRONICS, ELECTRICAL ENGINEERING AND TELECOMMUNICATIONS

The Union of Electronics, Electrical Engineering and Telecommunications /CEEC/ is a Bulgarian scientific-technical, non-governmental, non-political, and non-profit creative and professional association – it is an integral part of the civil society in the Republic of Bulgaria and the European Union. CEEC has always been an active member of the Federation of Scientific and Technical Unions in Bulgaria /FNTS/. CEEC is a full participating member of the Convention of National Societies of Electrical Engineers in Europe /EUREL/.

In the form of a professional association CEEC has existed under various names ever since 1936. In the beginning, as the division of Electrical Engineering in the National Organization of the Bulgarian Engineers and Architects /BIAD/, one of the oldest Bulgarian professional organizations.

CEEC has structures in all major cities in Bulgaria. Members of CEEC are more than 750 certified engineers, scientists teaching at the Technical Universities and the Bulgarian Academy of Sciences, specialists and managers working in factories and firms, students and post-graduate students, all organized in clubs and national scientific-technical divisions, dedicated to the fields in the industry of electrical engineering, telecommunications, electromagnetic compatibility, electronics, acoustics, etc. The corporate members include more than 20 companies, institutions and organizations.

CEEC is the principle organizer of several national and international scientific-technical events, such as the well-attended biannual conferences: the International Symposium on Electrical Apparatus and Technologies “SIELA”, the International Conference on Electrical Machines, Drives and Power systems “ELMA”, the International Conference on e-Beam Technologies “EBT”, the annual conferences “ELECTRONICS” and International conference “TELECOM”, the National conference with international participation “ACOUSTICS”, and the very popular with the young engineers Student Career Forum.

For over half a century CEEC has been the publisher of the peer-reviewed monthly scientific journal “ELECTROTECHNICA+ELECTRONICA” –“E+E”. The journal website is http:// epluse.fnts.bg

CEEC’s office is situated at: 108 Rakovski St., 1000 Sofia, BULGARIA
☎ +(359) 2 987 9767, email: ceec@mail.bg, web: http://ceec.fnts.bg